Comput. Mech. (2006) 38: 133–150
DOI 10.1007/s00466-005-0726-x

ORIGINAL PAPER

B. N. Rao · S. Rahman

A continuum shape sensitivity method for fracture analysis of isotropic functionally graded materials

Received: 6 January 2005 / Accepted: 8 June 2005 / Published online: 21 October 2005

Abstract This paper presents a new continuum shape sensitivity method for calculating mixed-mode stress-intensity factors for a stationary crack in two-dimensional, linear-elastic, isotropic FGMs with arbitrary geometry. The method involves the material derivative concept taken from continuum mechanics, the mutual potential energy release rate, and direct differentiation. Since the governing variational equation is differentiated prior to discretization, resulting sensitivity equations are independent of approximate numerical techniques, such as the finite element method, boundary element method, mesh-free method, or others. The discrete form of the mutual potential energy release rate is simple and easy to calculate, as it only requires multiplication of displacement vectors and stiffness sensitivity matrices. By judiciously selecting the velocity field, the method only requires displacement response in a subdomain close to the crack tip, thus making the method computationally efficient. Seven finite-element based numerical examples, which comprise mode-I and mixed-mode deformations and/or single or multiple interacting cracks, are presented to evaluate the accuracy of the fracture parameters calculated by the proposed method. Comparisons have been made between stress-intensity factors predicted by the proposed method and available reference solutions in the literature, generated either analytically or numerically using various other fracture integrals or analyses. Excellent agreement is obtained between the results of the proposed method and previously obtained solutions. Therefore, shape sensitivity analysis provides an attractive alternative to fracture analysis of cracks in homogeneous and non-homogeneous materials.

Keywords Crack · Functionally graded materials · Shape sensitivity analysis · Velocity field · Material derivative · Finite element method · Stress-intensity factor · Potential energy release rate

B. N. Rao (✉)
Structural Engineering Division,
Department of Civil Engineering,
Indian Institute of Technology, Madras,
Chennai, 600 036, India
Tel: 91-44-22574285
Fax: 91-44-22575286
E-mail: bnrao@iitm.ac.in

S. Rahman
Department of Mechanical and Industrial Engineering,
The University of Iowa,
Iowa City, IA 52242, USA
Tel: 1-319-335-5679
Fax: 1-319-335-5669
E-mail: rahman@engineering.uiowa.edu

1 Introduction

Functionally graded materials (FGMs) that possess a spatially varying microstructure and mechanical/thermal properties are essentially multi-phase particulate composites, engineered to meet a predetermined functional performance [1,2]. In recent years, various theoretical, computational, and experimental studies have been conducted to understand the fracture behavior of FGMs. A collection of technical papers, published in Volume 69, Issues 14–16 of [3] *Engineering Fracture Mechanics* (2002) reflects such state-of-the-art research into FGM fracture. A major component of such studies involves calculating crack-driving forces in FGMs accurately and efficiently. Consequently, various numerical methods have been developed or examined to calculate stress-intensity factors (SIFs), such as the displacement correlation method, the modified crack-closure integral method, the J_k^*-integral method and others [3]. More recently in 2003, the authors [4,5] developed two new interaction integrals for mixed-mode fracture analysis of cracks in both isotropic and orthotropic FGMs. In contrast to existing methods, it is not necessary to perform integration along the crack face of the discontinuity. Hence, the interaction integral method is simpler and more efficient than previously existing methods. Nevertheless, the majority of current numerical methods for FGM fracture analysis stem from extensions to methods originally developed for cracks in homogeneous materials.

An alternative approach to previously developed methods involves shape sensitivity analysis, which is frequently

employed in structural design optimization. Shape sensitivity analysis permits direct, analytical evaluation of first-order (and higher-order, if required) derivatives of potential energy with respect to crack size. Broadly speaking, there are two fundamentally different approaches to shape sensitivity analysis. The first, known as the discrete approach, employs a discretized numerical model (e.g., finite element method [FEM], boundary element method [BEM], mesh-free method, etc.) to approximate the potential energy and then transforms shape derivatives into differentiations of algebraic equations by controlling node motions. The second, known as the continuum approach and adopted in the present work, relies on the variational formulation used in continuum mechanics [6]. In this approach, shape sensitivity analysis is conducted by introducing a smooth velocity field to simulate shape change of the initial domain due to the crack advance. While discrete and continuum approaches are related (the former is an approximation of the latter), the continuum approach has two principal advantages: (1) a rigorous mathematical theory is obtained, without the uncertainty/errors associated with finite-dimensional approximation errors; and (2) explicit relations for sensitivity are obtained in terms of physical quantities rather than in terms of sums of derivatives of element matrices. These characteristic features of the continuum approach are of major importance in developing structural optimization theory [7, 8].

For homogeneous materials, several shape sensitivity methods involving discrete [9–11] and continuum [12–15] formulations have appeared in calculating SIFs. Both FEM and BEM have been employed for the shape sensitivity analysis of cracks. Most of these investigations are applicable only to linear-elastic fracture-mechanics problems. More recently, continuum shape sensitivity methods have also been developed for predicting first-order sensitivities of mixed-mode SIFs for isotropic materials [16–18]. These analytical sensitivities of SIFs provide a convenient means by which subsequent fracture reliability analysis can be performed accurately and efficiently. However, all of the aforementioned shape sensitivity methods are strictly applicable to homogeneous materials. As a result, there is considerable desire to develop shape sensitivity methods for the numerical evaluation of crack-driving forces in FGM, which is a major motivation of the present work.

This paper presents a continuum shape sensitivity method for calculating mixed-mode SIFs for a stationary crack in two-dimensional, linear-elastic, isotropic FGMs of arbitrary geometry. The method involves using the material derivative concept from continuum mechanics, the mutual potential energy release rate, and direct differentiation. Since the governing variational equation is differentiated prior to discretization, resulting sensitivity equations are independent of approximate numerical techniques, such as FEM, BEM, the mesh-free method, or others. Seven numerical examples in conjunction with FEM are presented to evaluate the accuracy of fracture parameters calculated by the proposed method. Comparisons have been made between the SIFs predicted by the proposed method and available reference solutions in the literature, generated either analytically or numerically using various other fracture integrals or analyses.

2 Crack tip fields in FGM

Consider a two-dimensional structure with a rectilinear crack of length $2a$, subjected to external loads $S_1, S_2, \ldots, S_M$, as shown in Fig. 1. It is assumed that the material properties, such as the modulus of elasticity E and the Poisson's ratio ν, vary according to

$$E = E(x_1, x_2) = E(\mathbf{x}) \tag{1}$$

and

$$\nu = \nu(x_1, x_2) = \nu(\mathbf{x}), \tag{2}$$

where $\mathbf{x} = \{x_1, x_2\}^{\mathrm{T}} \in \Re^2$, $E(\mathbf{x}) \geq 0$ and $-1 \leq \nu(\mathbf{x}) \leq 1/2$ are continuous, bounded, and at least piecewise differentiable functions on domain Ω. The $x_1 - x_2$ coordinate system is defined in Fig. 1. In reality, FGMs are multiphase materials with generally, locally discontinuous material properties. Hence, $E(\mathbf{x})$ and $\nu(\mathbf{x})$ in Eqs. (1) and (2) should be viewed as smoothly varying "effective" material properties of FGMs. In this case, FGMs can be modeled as non-homogeneous materials, for which the elastic constitutive equation is

$$\varepsilon_{ij} = \frac{1+\nu^*(\mathbf{x})}{E^*(\mathbf{x})}\sigma_{ij} + \frac{\nu^*(\mathbf{x})}{E^*(\mathbf{x})}\sigma_{kk}\delta_{ij}, \tag{3}$$

where ε_{ij} and σ_{ij} are the strain and stress components, respectively, and δ_{ij} is the Kronecker delta. In Eq. (3), $E^*(\mathbf{x})$ and $\nu^*(\mathbf{x})$ are given by $E(\mathbf{x})$ and $\nu(\mathbf{x})$ under the plane stress condition and by $E(\mathbf{x})/\left[1-\nu(\mathbf{x})^2\right]$ and $\nu(\mathbf{x})/[1-\nu(\mathbf{x})]$ under the plane strain condition, respectively. For non-homogeneous materials undergoing plane stress or plane strain linear-elastic deformation in the absence of body forces, the Airy stress function $F(x_1, x_2)$ satisfies [19]

$$\begin{aligned}\nabla^2\left(\frac{\nabla^2 F}{E^*(\mathbf{x})}\right) &- \frac{\partial^2}{\partial x_2^2}\left(\frac{1+\nu^*(\mathbf{x})}{E^*(\mathbf{x})}\right)\frac{\partial^2 F}{\partial x_1^2} \\ &- \frac{\partial^2}{\partial x_1^2}\left(\frac{1+\nu^*(\mathbf{x})}{E^*(\mathbf{x})}\right)\frac{\partial^2 F}{\partial x_2^2} \\ &+ 2\frac{\partial^2}{\partial x_1 \partial x_2}\left(\frac{1+\nu^*(\mathbf{x})}{E^*(\mathbf{x})}\right)\frac{\partial^2 F}{\partial x_1 \partial x_2} = 0,\end{aligned} \tag{4}$$

where $\nabla^2 = \partial^2/\partial x_1^2 + \partial^2/\partial x_2^2$ is the two-dimensional Laplacian operator. Eischen [19] showed that upon expanding Eq. (4), the first term in the governing differential equation for F involves the biharmonic term identical to the homogeneous material, while remaining terms involve spatial derivatives of the elastic moduli. Hence, the elastic stress and displacement fields in FGM can be derived using the stress function in variable separable form, identical to the homogeneous case. Hence, the linear-elastic singular stress field near the crack tip can be obtained as [19]

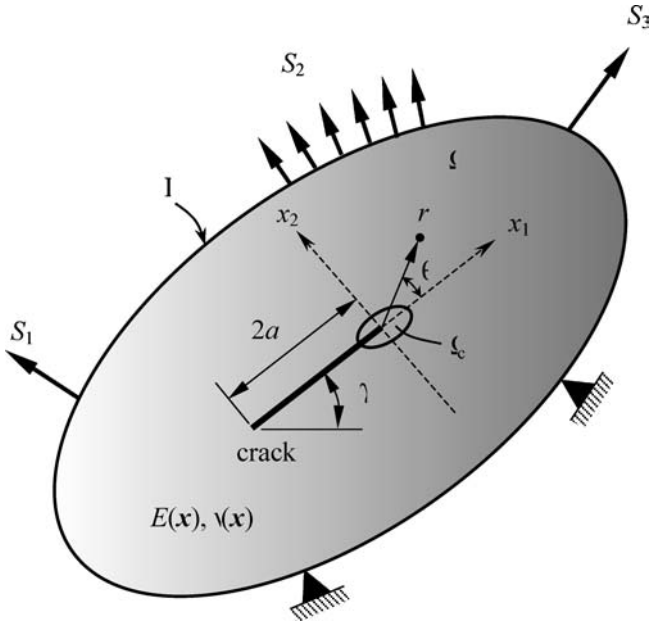

Fig. 1 A crack in a functionally graded material

$$\sigma_{11} = \frac{1}{\sqrt{2\pi r}}\left[K_I f_{11}^I(\theta) + K_{II} f_{11}^{II}(\theta)\right]$$
$$\sigma_{22} = \frac{1}{\sqrt{2\pi r}}\left[K_I f_{22}^I(\theta) + K_{II} f_{22}^{II}(\theta)\right], \quad (5)$$
$$\sigma_{12} = \frac{1}{\sqrt{2\pi r}}\left[K_I f_{12}^I(\theta) + K_{II} f_{12}^{II}(\theta)\right]$$

where K_I and K_{II} are the mode-I and mode-II SIFs, respectively, and $f_{ij}^I(\theta)$ and $f_{ij}^{II}(\theta)$ $(i, j = 1, 2)$ are the standard angular functions for a crack in a homogeneous elastic medium. Similarly, the near tip displacement field $\mathbf{z} = \{z_1, z_2\}^{\mathrm{T}}$ can be obtained as [19]

$$z_1 = \frac{1}{\mu_{\text{tip}}}\sqrt{\frac{r}{2\pi}}\left[K_I g_1^I(\theta) + K_{II} g_1^{II}(\theta)\right]$$
$$z_2 = \frac{1}{\mu_{\text{tip}}}\sqrt{\frac{r}{2\pi}}\left[K_I g_2^I(\theta) + K_{II} g_2^{II}(\theta)\right], \quad (6)$$

where $\mu_{\text{tip}} = E_{\text{tip}}\Big/\left[2\left(1+\nu_{\text{tip}}\right)\right]$ is the shear modulus, $E_{\text{tip}}$is the elastic modulus, and ν_{tip} is Poisson's ratio, all evaluated at the crack tip; $g_i^I(\theta)$and $g_i^{II}(\theta)$, $i = 1, 2$ are standard angular functions for a crack in a homogeneous elastic medium [20]. Even though the material gradient does not influence the square-root singularity or the singular stress distribution, the material gradient does affect the size of the region in which the homogeneous solution is valid.

3 Shape sensitivity analysis

3.1 Velocity field

Consider a general three-dimensional body with a specific configuration, referred to as the initial (reference) configuration, with domain Ω, boundary Γ, and a body material point identified by position vector $\mathbf{x} \in \Omega$. Consider the body's motion from an initial configuration with domain Ω and boundary Γ into a perturbed configuration with domain Ω_τ and boundary Γ_τ, as shown in Fig. 2. This process can be expressed as

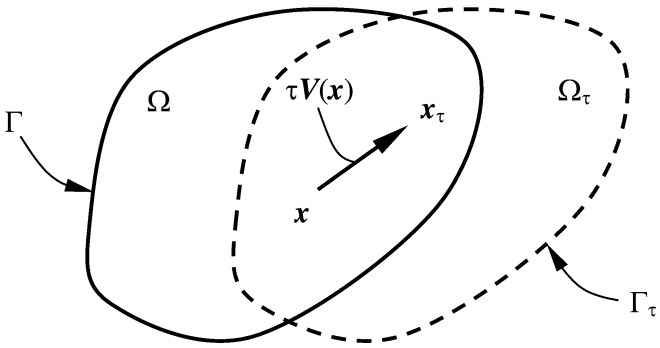

Fig. 2 Variation of domain

$$\mathbf{T}{:}\mathbf{x} \to \mathbf{x}_\tau, \quad \mathbf{x} \in \Omega, \quad (7)$$

where $\mathbf{x}_\tau$ is the position vector of the material point in the perturbed configuration, $\mathbf{T}$ is a transformation mapping, and $\tau \in \mathbb{R}^+$ is a scalar, fictitious, time-like parameter denoting the amount of shape change, with

$$\begin{aligned}\mathbf{x}_\tau &= \mathbf{T}(\mathbf{x}, \tau)\\ \Omega_\tau &= \mathbf{T}(\Omega, \tau).\\ \Gamma_\tau &= \mathbf{T}(\Gamma, \tau)\end{aligned} \quad (8)$$

A velocity field can then be defined as

$$\mathbf{v}(\mathbf{x}_\tau, \tau) \equiv \frac{\mathrm{d}\mathbf{x}_\tau}{\mathrm{d}\tau} = \frac{\mathrm{d}\mathbf{T}(\mathbf{x}, \tau)}{\mathrm{d}\tau} = \frac{\partial \mathbf{T}(\mathbf{x}, \tau)}{\partial \tau}. \quad (9)$$

In the neighborhood of the initial time $\tau = 0$, assuming a regularity hypothesis and ignoring high-order terms,

$$\begin{aligned}\mathbf{x}_\tau = \mathbf{T}(\mathbf{x}, \tau) &= \mathbf{T}(\mathbf{x}, 0) + \tau\frac{\partial \mathbf{T}(\mathbf{x}, 0)}{\partial \tau} + O\left(\tau^2\right)\\ &\cong \mathbf{x} + \tau\mathbf{v}(\mathbf{x}, 0),\end{aligned} \quad (10)$$

where $\mathbf{x} = \mathbf{T}(\mathbf{x}, 0)$. For the rest of this paper, the velocity field $\mathbf{v}(\mathbf{x}, 0)$ will be denoted by $\mathbf{V}(\mathbf{x})$ or $\mathbf{V}$. Thus, a velocity field characterizes the direction of domain variation, which implies that for a given $\mathbf{V}(\mathbf{x})$, the shape change of Ω is uniquely controlled by the scalar parameter τ.

3.2 Sensitivity analysis

The variational governing equation for a linear-elastic, nonhomogeneous or homogeneous solid with domain Ω can be formulated as [8]

$$a_\Omega(\mathbf{z}, \bar{\mathbf{z}}) = \ell_\Omega(\bar{\mathbf{z}}), \quad \text{for all } \bar{\mathbf{z}} \in \mathbf{Z} \quad (11)$$

where $\mathbf{z}$ and $\bar{\mathbf{z}}$ are the actual and virtual displacement fields of the structure, respectively, $\mathbf{Z}$ is the space of kinematically admissible virtual displacements, and $a_\Omega(\mathbf{z}, \bar{\mathbf{z}})$ and $\ell_\Omega(\bar{\mathbf{z}})$ are

energy bilinear and load linear forms, respectively. The subscript Ω in Eq. (11) is used to indicate the dependency of the governing equation on the shape of the structural domain. If $\mathbf{z}_\tau(\mathbf{x}_\tau)$ represents the displacement at $\mathbf{x}_\tau = \mathbf{x} + \tau\mathbf{V}(\mathbf{x})$ of the perturbed domain, the pointwise material derivative at $\mathbf{x} \in \Omega$ is defined as [8]

$$\dot{\mathbf{z}}(\mathbf{x}) \equiv \lim_{\tau\to 0}\left[\frac{\mathbf{z}_\tau(\mathbf{x}+\tau\mathbf{V}(\mathbf{x})) - \mathbf{z}(\mathbf{x})}{\tau}\right] = \mathbf{z}'(\mathbf{x}) + \nabla\mathbf{z}^{\mathrm{T}}\mathbf{V}(\mathbf{x}) \quad . \tag{12}$$

where

$$\mathbf{z}' = \lim_{\tau\to 0}\left[\frac{\mathbf{z}_\tau(\mathbf{x}) - \mathbf{z}(\mathbf{x})}{\tau}\right] \tag{13}$$

is the partial derivative of $\mathbf{z}$ and $\nabla = \left\{\partial/\partial x_1, \partial/\partial x_2, \partial/\partial x_3\right\}^{\mathrm{T}}$ is the vector of gradient operators.

If no body forces are involved, the variational equation (Eq. (11)) can be written as

$$a_\Omega(\mathbf{z}, \bar{\mathbf{z}}) \equiv \int_\Omega \sigma_{ij}(\mathbf{z})\varepsilon_{ij}(\bar{\mathbf{z}})\mathrm{d}\Omega = \ell_\Omega(\bar{\mathbf{z}}) \equiv \int_\Gamma T_i\bar{z}_i\,\mathrm{d}\Gamma, \tag{14}$$

where $\sigma_{ij}(\mathbf{z})$ and $\varepsilon_{ij}(\bar{\mathbf{z}})$ are components of the stress and strain tensors of the displacement $\mathbf{z}$ and virtual displacement $\bar{\mathbf{z}}$, respectively, T_i is the ith component of the surface traction, and $\bar{z}_i$ is the ith component of $\bar{\mathbf{z}}$. Taking the material derivative of both sides of Eq. (14), it can be shown that [8]

$$a_\Omega(\dot{\mathbf{z}}, \bar{\mathbf{z}}) = \ell'_{\mathbf{V}}(\bar{\mathbf{z}}) - a'_{\mathbf{V}}(\mathbf{z}, \bar{\mathbf{z}}), \quad \forall\,\bar{\mathbf{z}} \in \mathbf{Z} \tag{15}$$

where the subscript $\mathbf{V}$ indicates the dependency of the terms on the velocity field. The terms $\ell'_{\mathbf{V}}(\bar{\mathbf{z}})$ and $a'_{\mathbf{V}}(\mathbf{z}, \bar{\mathbf{z}})$ can be further derived as [8]

$$\ell'_{\mathbf{V}}(\bar{\mathbf{z}}) = \int_\Gamma \left\{-T_i\left(\bar{z}_{i,j}V_j\right) + \left[(T_i\bar{z}_i)_{,j} + n_j + \kappa_\Gamma(T_i\bar{z}_i)\right](V_i n_i)\right\}\mathrm{d}\Gamma \tag{16}$$

and

$$a'_{\mathbf{V}}(\mathbf{z}, \bar{\mathbf{z}}) = -\int_\Omega \begin{bmatrix} \varepsilon_{ij}(\mathbf{z})D_{ijkl}(\mathbf{x})(\bar{z}_{k,m}\mathbf{V}_{m,l}) \\ +\varepsilon_{ij}(\bar{\mathbf{z}})D_{ijkl}(\mathbf{x})(z_{k,m}\mathbf{V}_{m,l}) \\ -\varepsilon_{ij}(\bar{\mathbf{z}})D_{ijkl,m}(\mathbf{x})\varepsilon_{kl}(\mathbf{z})V_m \\ -\varepsilon_{ij}(\mathbf{z})D_{ijkl}(\mathbf{x})\varepsilon_{kl}(\bar{\mathbf{z}})\mathrm{div}\mathbf{V} \end{bmatrix}\mathrm{d}\Omega, \tag{17}$$

where n_i is the ith component of unit normal vector $\mathbf{n}$, κ_Γ is the curvature of the boundary, $z_{i,j} = \partial z_i/\partial x_j$, $\bar{z}_{i,j} = \partial\bar{z}_i/\partial x_j$, $V_{i,j} = \partial V_i/\partial x_j$, $D_{ijkl}(\mathbf{x})$ is a component of the constitutive tensor and $D_{ijkl,m}(\mathbf{x}) = \partial D_{ijkl}(\mathbf{x})/\partial x_m$. If the modulus of elasticity $E(\mathbf{x})$ is the only material property that varies, then $D_{ijkl,m}(\mathbf{x}) = \left[\partial E(\mathbf{x})/\partial x_m\right] D_{ijkl}(\mathbf{x})/E(\mathbf{x})$. Note that the third term in the integrand on the right hand side of Eq. (17) arises naturally in the formulation of a continuum shape sensitivity analysis for non-homogeneous materials, but vanishes for homogeneous materials. In addition, D_{ijkl} is constant for homogeneous materials.

4 Shape sensitivity method for fracture analysis

Mutual potential energy is an effective fracture response for calculating mixed-mode SIFs in homogeneous materials [4, 5]. In this section, mutual potential energy and its material derivative is first derived in conjunction with continuum shape sensitivity analysis to solve mixed-mode problems in homogeneous materials. The procedure is then extended for cracks in FGM. In fact, the study of FGM would enhance the understanding of a fracture in a generic material, since upon shrinking the gradient layer in FGM is expected to behave like a sharp interface, and upon expansion, the fracture behavior would be analogous to that of a homogeneous material.

4.1 Homogeneous materials

Consider an arbitrary, two-dimensional cracked body of crack length a, with unit thickness subjected to an arbitrary loading. The total potential energy Π of the system in the absence of body forces is

$$\Pi \equiv \frac{1}{2}\int_\Omega \varepsilon_{ij}(\mathbf{z})D_{ijkl}\varepsilon_{kl}(\mathbf{z})\mathrm{d}\Omega - \int_\Gamma T_i z_i\,\mathrm{d}\Gamma, \tag{18}$$

where, for two-dimensional linear elastic material models, D_{ijkl}, are the components of the constant elasticity matrix

$$\mathbf{D} = \begin{cases} \frac{E}{1-\nu^2}\begin{bmatrix} 1 & \nu & 0 \\ \nu & 1 & 0 \\ 0 & 0 & \frac{1-\nu}{2} \end{bmatrix}, & \text{for plane stress} \\ \frac{E}{[1+\nu][1-2\nu]}\begin{bmatrix} 1-\nu & \nu & 0 \\ \nu & 1-\nu & 0 \\ 0 & 0 & \frac{1-2\nu}{2} \end{bmatrix}, & \text{for plane strain} \end{cases} \tag{19}$$

By substituting $\bar{\mathbf{z}}$ with $\mathbf{z}$ in Eq. (14) and by using Eq. (18), the following is produced

$$\Pi = -\frac{1}{2}a_\Omega(\mathbf{z}, \mathbf{z}). \tag{20}$$

The energy release rate is equal to the derivative of potential energy with respect to the crack area. For a two-dimensional cracked structure with unit thickness, the crack area is equal to crack length a. Assuming crack length a to be the variable of interest, a change in crack area or crack length involves a change in the shape of the cracked continuum. In relation to shape sensitivity theory, such a change implies that the energy release rate is equal to the material derivative of potential energy. Hence, for elastic (linear or nonlinear) solids under mixed-mode loading conditions, the J-integral, which is equal to the energy release rate, can be derived as

$$J \equiv -\dot{\Pi} = \frac{1}{2}\left[a_\Omega(\dot{\mathbf{z}}, \mathbf{z}) + a_\Omega(\mathbf{z}, \dot{\mathbf{z}}) + a'_{\mathbf{V}}(\mathbf{z}, \mathbf{z})\right], \tag{21}$$

where the overdot indicates a material derivative. If (1) velocity field $\mathbf{V}(\mathbf{x})$ is defined such that traction-loading boundary Γ is fixed, i.e., $\mathbf{V}(\mathbf{x}) = \mathbf{0}$ on the traction-loading boundary Γ; and (2) $\bar{\mathbf{z}}$ is replaced with $\mathbf{z}$ in Eq. (15), noting that $a_\Omega(\dot{\mathbf{z}}, \mathbf{z}) = a_\Omega(\mathbf{z}, \dot{\mathbf{z}}) = -a'_{\mathbf{V}}(\mathbf{z}, \mathbf{z})$, then

$$J = -\frac{1}{2}a'_{\mathbf{V}}(\mathbf{z}, \mathbf{z}). \tag{22}$$

Substituting the expression of $a'_{\mathbf{V}}(\mathbf{z}, \mathbf{z})$ from Eq. (17) and noting that D_{ijkl} is constant for homogeneous materials

($D_{ijkl,m} = 0$) gives

$$J = \frac{1}{2}\int_{\Omega}\left[\sigma_{ij}(\mathbf{z})(z_{i,k}V_{k,j}) + \sigma_{ij}(\mathbf{z})(z_{i,k}V_{k,j}) - \sigma_{ij}(\mathbf{z})\varepsilon_{ij}(\mathbf{z})\mathrm{div}\ \mathbf{V}\right]\mathrm{d}\Omega. \tag{23}$$

Defining $W = \sigma_{ij}\varepsilon_{ij}/2$ as the strain energy density and $\mathbf{V}(\mathbf{x}) = \{V_1(\mathbf{x}), 0\}^{\mathrm{T}}$ as the velocity field, with $V_1(\mathbf{x})$ having a value of unity at the crack tip, zero along the boundary of the domain, and arbitrary elsewhere, the following is produced

$$J = \int_{\Omega}\left(\sigma_{ij}\frac{\partial z_i}{\partial x_1} - W\delta_{1j}\right)\frac{\partial V_1}{\partial x_j}\mathrm{d}\Omega \tag{24}$$

which is the same as the traditional domain form of the J-integral, with V_1 taking the place of weight function q. Hence, weight function q can be considered the virtual change in crack length, having a value of unity at the crack tip, zero along the boundary of the domain, and arbitrary elsewhere.

Now, consider two independent equilibrium states of the cracked body. Let state 1 correspond to the actual state for given boundary conditions, and let state 2 correspond to an auxiliary state, which can be either mode-I or mode-II near crack tip displacement and stress fields for homogeneous materials [20]. Superposition of these two states leads to another equilibrium state (state S) for which the total potential energy $\Pi^{(S)}$ is

$$\Pi^{(S)} = \frac{1}{2}\int_{\Omega}\varepsilon_{ij}\left(\mathbf{z}^{(1)} + \mathbf{z}^{(2)}\right)D_{ijkl}\varepsilon_{kl}\left(\mathbf{z}^{(1)} + \mathbf{z}^{(2)}\right)\mathrm{d}\Omega - \int_{\Gamma}\left(T_i^{(1)} + T_i^{(2)}\right)\left(z_i^{(1)} + z_i^{(2)}\right)\mathrm{d}\Gamma, \tag{25}$$

where $z_i^{(1)}$, $T_i^{(1)}$ are the components of displacement and external force vectors, respectively, of the actual state for given boundary conditions, and $z_i^{(2)}$, $T_i^{(2)}$ are the components of displacement and external force vectors, respectively, of the auxiliary state. By using the divergence theorem,

$$\int_{\Gamma}\left(T_i^{(1)}\right)\left(z_i^{(1)}\right)\mathrm{d}\Gamma = \int_{\Omega}\varepsilon_{ij}(\mathbf{z}^{(1)})D_{ijkl}\varepsilon_{kl}(\mathbf{z}^{(1)})\mathrm{d}\Omega, \tag{26}$$

$$\int_{\Gamma}\left(T_i^{(2)}\right)\left(z_i^{(2)}\right)\mathrm{d}\Gamma = \int_{\Omega}\varepsilon_{ij}(\mathbf{z}^{(2)})D_{ijkl}\varepsilon_{kl}(\mathbf{z}^{(2)})\mathrm{d}\Omega, \tag{27}$$

$$\int_{\Gamma}\left(T_i^{(1)}\right)\left(z_i^{(2)}\right)\mathrm{d}\Gamma = \int_{\Omega}\varepsilon_{ij}(\mathbf{z}^{(1)})D_{ijkl}\varepsilon_{kl}(\mathbf{z}^{(2)})\mathrm{d}\Omega, \tag{28}$$

and

$$\int_{\Gamma}\left(T_i^{(2)}\right)\left(z_i^{(1)}\right)\mathrm{d}\Gamma = \int_{\Omega}\varepsilon_{ij}(\mathbf{z}^{(2)})D_{ijkl}\varepsilon_{kl}(\mathbf{z}^{(1)})\mathrm{d}\Omega, \tag{29}$$

which, when applied to the expanded form of Eq. (25) yields

$$\Pi^{(S)} = \Pi^{(1)} + \Pi^{(2)} + \Pi^{(1,2)}, \tag{30}$$

where

$$\Pi^{(1)} = -\frac{1}{2}a_{\Omega}\left(\mathbf{z}^{(1)}, \mathbf{z}^{(1)}\right), \tag{31}$$

$$\Pi^{(2)} = -\frac{1}{2}a_{\Omega}\left(\mathbf{z}^{(2)}, \mathbf{z}^{(2)}\right), \tag{32}$$

and

$$\Pi^{(1,2)} = -\frac{1}{2}a_{\Omega}\left(\mathbf{z}^{(1)}, \mathbf{z}^{(2)}\right) - \frac{1}{2}a_{\Omega}\left(\mathbf{z}^{(2)}, \mathbf{z}^{(1)}\right) \tag{33}$$

are various potential energies with

$$a_{\Omega}\left(\mathbf{z}^{(i)}, \mathbf{z}^{(j)}\right) = \int_{\Omega}\varepsilon_{ij}(\mathbf{z}^{(1)})D_{ijkl}\varepsilon_{kl}(\mathbf{z}^{(j)})\mathrm{d}\Omega; \quad i, j = 1, 2. \tag{34}$$

Hence, the J-integral for the superposed state, denoted by $J^{(S)}$, can be obtained as

$$J^{(S)} \equiv -\dot{\Pi}^{(S)} = -\dot{\Pi}^{(1)} - \dot{\Pi}^{(2)} - \dot{\Pi}^{(1,2)}. \tag{35}$$

Again, if the velocity field is defined such that $\mathbf{V}(\mathbf{x}) = \mathbf{0}$ on the traction-loading boundary Γ and under similar considerations, $a_{\Omega}\left(\mathbf{z}^{(i)}, \mathbf{z}^{(j)}\right) = a_{\Omega}\left(\mathbf{z}^{(i)}, \mathbf{z}^{(j)}\right) = -a'_{\mathbf{V}}\left(\mathbf{z}^{(i)}, \mathbf{z}^{(j)}\right)$; $i, j = 1, 2$, yielding

$$J^{(S)} = -\frac{1}{2}a'_{\mathbf{V}}\left(\mathbf{z}^{(1)}, \mathbf{z}^{(1)}\right) - \frac{1}{2}a'_{\mathbf{V}}\left(\mathbf{z}^{(2)}, \mathbf{z}^{(2)}\right) - \frac{1}{2}a'_{\mathbf{V}}\left(\mathbf{z}^{(1)}, \mathbf{z}^{(2)}\right) - \frac{1}{2}a'_{\mathbf{V}}\left(\mathbf{z}^{(2)}, \mathbf{z}^{(1)}\right). \tag{36}$$

On further expansion, $J^{(S)}$ can be decomposed to

$$J^{(S)} = J^{(1)} + J^{(2)} + M^{(1,2)} \tag{37}$$

where

$$J^{(1)} = -\dot{\Pi}^{(1)} = -\frac{1}{2}a'_{\mathbf{V}}\left(\mathbf{z}^{(1)}, \mathbf{z}^{(1)}\right) \tag{38}$$

and

$$J^{(2)} = -\dot{\Pi}^{(2)} = -\frac{1}{2}a'_{\mathbf{V}}\left(\mathbf{z}^{(2)}, \mathbf{z}^{(2)}\right) \tag{39}$$

are the J-integrals for states 1 and 2, respectively, noting that $a'_{\mathbf{V}}\left(\mathbf{z}^{(1)}, \mathbf{z}^{(2)}\right) = a'_{\mathbf{V}}\left(\mathbf{z}^{(2)}, \mathbf{z}^{(1)}\right)$,

$$M^{(1,2)} = -\dot{\Pi}^{(1,2)} = -a'_{\mathbf{V}}\left(\mathbf{z}^{(1)}, \mathbf{z}^{(2)}\right) \tag{40}$$

is the mutual potential energy release rate. By replacing $\mathbf{z}$, and $\bar{\mathbf{z}}$ in Eq. (17) with $\mathbf{z}^{(1)}$, and $\mathbf{z}^{(2)}$respectively, and assuming $\mathbf{V}(\mathbf{x}) = V_1(\mathbf{x})$ having a value of unity at the crack tip, zero along the boundary of the domain, and arbitrary elsewhere, the following is obtained

$$M^{(1,2)} = \int_{\Omega}\left[\sigma_{ij}\left(\mathbf{z}^{(1)}\right)\frac{\partial z_i^{(2)}}{\partial x_1} + \sigma_{ij}\left(\mathbf{z}^{(2)}\right)\frac{\partial z_i^{(1)}}{\partial x_1} - W^{(1,2)}\delta_{1j}\right]\frac{\partial V_1}{\partial x_j}\mathrm{d}\Omega \tag{41}$$

where $W^{(1,2)} = \left[\sigma_{ij}\left(\mathbf{z}^{(1)}\right)\varepsilon_{ij}\left(\mathbf{z}^{(2)}\right) + \sigma_{ij}\left(\mathbf{z}^{(2)}\right)\varepsilon_{ij}\left(\mathbf{z}^{(1)}\right)\right]/2$ is the mutual strain energy density. Again, $M^{(1,2)}$ in Eq. (41) is same as the domain form of the M-integral (interaction integral) for the mixed-mode fracture of homogeneous materials, with V_1 taking the place of weight function q. In fact, various fracture integrals can be derived using shape sensitivity analysis.

4.2 Functionally graded materials

As with the treatment of homogeneous materials, consider two independent equilibrium states of an FGM cracked structure. Let state 1 correspond to the actual state for given boundary conditions. Let state 2 correspond to an auxiliary state, which can be either mode-I or mode-II near tip displacement and stress fields. Superposition of these two states leads to another equilibrium state (state S) for which the total potential energy, henceforth referred to as $\tilde{\Pi}^{(S)}$, is

$$\tilde{\Pi}^{(S)} = \frac{1}{2}\int_{\Omega} \varepsilon_{ij}\left(\mathbf{z}^{(1)}+\mathbf{z}^{(2)}\right) D_{ijkl}(\mathbf{x})\varepsilon_{kl}\left(\mathbf{z}^{(1)}+\mathbf{z}^{(2)}\right) \mathrm{d}\Omega - \int_{\Gamma}\left(T_i^{(1)}+T_i^{(2)}\right)\left(z_i^{(1)}+z_i^{(2)}\right)\mathrm{d}\Gamma. \tag{42}$$

For states 1 and S, $D_{ijkl}(\mathbf{x})$ varies as the function of spatial location and is given by Eq. (19) with E and ν replaced by $E(\mathbf{x})$ and $\nu(\mathbf{x})$ respectively. However, for state 2, which is the auxiliary state, a different constitutive matrix that satisfies both equilibrium and compatibility conditions must be defined. For state 2, define a D_{ijkl}^{aux} that can be obtained from Eq. (19) with E and ν replaced by E_{tip} and ν_{tip} respectively. It can be easily shown that the divergence theorem yields equations similar to Eqs. (26)–(29) with D_{ijkl} replaced by $D_{ijkl}(\mathbf{x})$ which, when applied to the expanded form of Eq. (42), gives

$$\tilde{\Pi}^{(S)} = \tilde{\Pi}^{(1)} + \tilde{\Pi}^{(2)} + \tilde{\Pi}^{(1,2)}, \tag{43}$$

where $\tilde{\Pi}^{(1)}$ is same as $\Pi^{(1)}$ given in Eq. (31), and

$$\tilde{\Pi}^{(2)} = -\frac{1}{2}a_{\Omega}^{\text{aux}}\left(\mathbf{z}^{(2)},\mathbf{z}^{(2)}\right), \tag{44}$$

$$\tilde{\Pi}^{(1,2)} = -a_{\Omega}\left(\mathbf{z}^{(1)},\mathbf{z}^{(2)}\right) - \frac{1}{2}a_{\Omega}\left(\mathbf{z}^{(2)},\mathbf{z}^{(2)}\right) + \frac{1}{2}a_{\Omega}^{\text{aux}}\left(\mathbf{z}^{(2)},\mathbf{z}^{(2)}\right), \tag{45}$$

with $a_{\Omega}\left(\mathbf{z}^{(1)},\mathbf{z}^{(2)}\right)$ and $a_{\Omega}\left(\mathbf{z}^{(2)},\mathbf{z}^{(2)}\right)$ given by Eq. (34) with D_{ijkl} replaced by $D_{ijkl}(\mathbf{x})$, and $a_{\Omega}^{\text{aux}}\left(\mathbf{z}^{(2)},\mathbf{z}^{(2)}\right)$ given by Eq. (34) with D_{ijkl} replaced by D_{ijkl}^{aux}. Hence, the J-integral for the superposed state, denoted as $\tilde{J}^{(S)}$, can be obtained from

$$\tilde{J}^{(S)} \equiv -\dot{\tilde{\Pi}}^{(S)} = -\dot{\tilde{\Pi}}^{(1)} - \dot{\tilde{\Pi}}^{(2)} - \dot{\tilde{\Pi}}^{(1,2)}. \tag{46}$$

If the velocity field is defined such that $\mathbf{V}(\mathbf{x}) = \mathbf{0}$ on the traction-loading boundary Γ, then $a_{\Omega}\left(\mathbf{z}^{(1)},\mathbf{z}^{(2)}\right) = -a'_{\mathbf{V}}\left(\mathbf{z}^{(1)},\mathbf{z}^{(2)}\right)$, $a_{\Omega}\left(\mathbf{z}^{(2)},\mathbf{z}^{(2)}\right) = -a'_{\mathbf{V}}\left(\mathbf{z}^{(2)},\mathbf{z}^{(2)}\right)$, and $a_{\Omega}^{\text{aux}}\left(\mathbf{z}^{(2)},\mathbf{z}^{(2)}\right) = -a'^{\text{aux}}_{\mathbf{V}}\left(\mathbf{z}^{(2)},\mathbf{z}^{(2)}\right)$. Hence, $\tilde{J}^{(S)}$ can be decomposed into

$$\tilde{J}^{(S)} = \tilde{J}^{(1)} + \tilde{J}^{(2)} + \tilde{M}^{(1,2)}, \tag{47}$$

in which $\tilde{J}^{(1)}$ and $\tilde{J}^{(2)}$are the $\tilde{J}$-integrals for states 1 and 2, respectively with $\tilde{J}^{(1)}$ being same as $J^{(1)}$ given in Eq. (38),

$$\tilde{J}^{(2)} = -\dot{\tilde{\Pi}}^{(2)} = -\frac{1}{2}a'^{\text{aux}}_{\mathbf{V}}\left(\mathbf{z}^{(2)},\mathbf{z}^{(2)}\right), \tag{48}$$

$$\tilde{M}^{(1,2)} = -\dot{\tilde{\Pi}}^{(1,2)} = -a'_{\mathbf{V}}\left(\mathbf{z}^{(1)},\mathbf{z}^{(2)}\right) + \frac{1}{2}\left[a'^{\text{aux}}_{\mathbf{V}}\left(\mathbf{z}^{(2)},\mathbf{z}^{(2)}\right) - a'_{\mathbf{V}}\left(\mathbf{z}^{(2)},\mathbf{z}^{(2)}\right)\right] \tag{49}$$

is the mutual potential energy release rate, where

$$a'_{\mathbf{V}}\left(\mathbf{z}^{(i)},\mathbf{z}^{(j)}\right) = -\int_{\Omega}\begin{bmatrix} \varepsilon_{ij}\left(\mathbf{z}^{(i)}\right) D_{ijkl}(\mathbf{x})\left(z_{k,m}^{(j)}V_{m,l}\right) \\ +\varepsilon_{ij}\left(\mathbf{z}^{(j)}\right) D_{ijkl}(\mathbf{x})\left(z_{k,m}^{(i)}V_{m,l}\right) \\ -\varepsilon_{ij}\left(\mathbf{z}^{(j)}\right) D_{ijkl,m}(\mathbf{x})\varepsilon_{kl}\left(z^{(i)}\right)V_m \\ -\varepsilon_{ij}\left(\mathbf{z}^{(i)}\right) D_{ijkl}(\mathbf{x})\varepsilon_{kl}\left(z^{(j)}\right)\mathrm{div}\mathbf{V} \end{bmatrix} d\Omega; \quad i,j=1,2 \tag{50}$$

and

$$a'^{\text{aux}}_{\mathbf{V}}\left(\mathbf{z}^{(2)},\mathbf{z}^{(2)}\right) = -\int_{\Omega}\begin{bmatrix} \varepsilon_{ij}\left(\mathbf{z}^{(2)}\right) D_{ijkl}^{\text{aux}}\left(z_{k,m}^{(2)}V_{m,l}\right) \\ +\varepsilon_{ij}\left(\mathbf{z}^{(2)}\right) D_{ijkl}^{\text{aux}}\left(z_{k,m}^{(2)}V_{m,l}\right) \\ -\varepsilon_{ij}\left(\mathbf{z}^{(2)}\right) D_{ijkl}^{\text{aux}}\varepsilon_{kl}\left(z^{(2)}\right)\mathrm{div}\mathbf{V} \end{bmatrix} d\Omega, \tag{51}$$

To evaluate all three terms of $\tilde{M}^{(1,2)}$ in Eq. (49), one needs to prescribe an appropriate velocity field $\mathbf{V}(\mathbf{x})$ and auxiliary displacement field $\mathbf{z}^{(2)}$; and calculate actual displacement field $\mathbf{z}^{(1)}$ for the initial shape of the cracked body. In other words, a single stress analysis employing a suitable numerical method, such as FEM or the mesh-free method, efficiently evaluates $\tilde{J}$- and $\tilde{M}$-integrals. In contrast to Eqs. (22) and (40), which lead to existing expressions of J- and M-integrals in homogeneous materials, respectively, Eq. (49) is new and applicable to general non-homogeneous materials. When both the elastic modulus and Poisson's ratio have no spatial variation, $a'^{\text{aux}}_{\mathbf{V}}\left(\mathbf{z}^{(2)},\mathbf{z}^{(2)}\right) = a'_{\mathbf{V}}\left(\mathbf{z}^{(2)},\mathbf{z}^{(2)}\right)$, the $\tilde{J}$- and $\tilde{M}$-integrals in Eqs. (48)–(49) degenerate into homogeneous solutions, as expected.

4.3 Stress intensity factors

The mutual potential energy release rate can also be represented in terms of mixed-mode stress intensity factors as [4,5]

$$\tilde{M}^{(1,2)} = \frac{2}{E^*_{tip}}\left[\left(K_I^{(1)}K_I^{(2)} + K_{II}^{(1)}K_{II}^{(2)}\right)\right], \tag{52}$$

where E^*_{tip} is equal to E^* evaluated at the crack tip. The individual SIFs for the actual state can be obtained by judiciously choosing the auxiliary state (state 2). For example, if state 2 is chosen to be state I, i.e., Eqs (5) and (6) with $K_I^{(2)} = 1$ and $K_{II}^{(2)} = 0$, then Eq. (52) can be reduced to

$$M^{(1,I)} = \frac{2K_I^{(1)}}{E^*}, \tag{53}$$

from which

$$K_I^{(1)} = \frac{M^{(1,I)}E^*}{2}. \tag{54}$$

Similarly, if state 2 is chosen to be state II, i.e., Eqs. (5) and (6), with $K_I^{(2)} = 0$ and $K_{II}^{(2)} = 1$, and similar considerations are followed, then

$$K_{II}^{(1)} = \frac{M^{(1,II)}E^*}{2}. \tag{55}$$

The mutual potential energy release rate $M^{(1,I)}$ and $M^{(1,II)}$ in Eqs. (54) and (55) can be evaluated from Eq. (49) by choosing the auxiliary state defined by Eqs. (5) and (6). In general, a numerical method is required for calculating $M^{(1,I)}$ and $M^{(1,II)}$.

5 Numerical Implementation

5.1 Finite element method

Consider a finite element discretization of a two-dimensional FGM cracked body involving N number of nodes. Let $\mathbf{z}_I^{(1)} \in \mathbb{R}^2$ and $\mathbf{z}_I^{(2)} \in \mathbb{R}^2$ be the actual and auxiliary displacement vectors, respectively, at the Ith node. If $\mathbf{d}^{(1)} = \left\{\mathbf{z}_I^{(1)}\right\} \in \mathbb{R}^{2N};\ I = 1, N$ and $\mathbf{d}^{(2)} = \left\{\mathbf{z}_I^{(2)}\right\} \in \mathbb{R}^{2N};\ I = 1, N$ represent global displacement vectors, the mutual potential energy release rate can be approximated by

$$\tilde{M}^{(1,2)} \cong \mathbf{d}^{(1)\mathrm{T}}\mathbf{K}'d^{(2)} + \frac{1}{2}\mathbf{d}^{(2)\mathrm{T}}\left(\mathbf{K}' - \mathbf{K}'^{\mathrm{aux}}\right)\mathbf{d}^{(2)}, \tag{56}$$

where $\mathbf{K}' = \left[\mathbf{k}'_{IJ}\right] \in L\left(\mathbb{R}^{2N} \times \mathbb{R}^{2N}\right);\ I, J = 1, N$ and $\mathbf{K}'^{\mathrm{aux}} = \left[\mathbf{k}'^{\mathrm{aux}}_{IJ}\right] \in L\left(\mathbb{R}^{2N} \times \mathbb{R}^{2N}\right)$ are two global stiffness sensitivity matrices with $\mathbf{k}'_{IJ} \in L\left(\mathbb{R}^2 \times \mathbb{R}^2\right)$ and $\mathbf{k}'^{\mathrm{aux}}_{IJ} \in L\left(\mathbb{R}^2 \times \mathbb{R}^2\right)$ representing element-level (domain Ω_e) sensitivity matrices, given by

$$\mathbf{k}'_{IJ} = \int_{\Omega_e} \left(\mathbf{B}_I^T\mathbf{D}(\mathbf{x})\mathbf{B}'_J + \mathbf{B}_I^T\mathbf{D}(\mathbf{x})\mathbf{B}'_J - \mathbf{B}_I^T\mathbf{D}'(\mathbf{x})\mathbf{B}_J - \mathbf{B}_I^T\mathbf{D}(\mathbf{x})\mathbf{B}_J\mathrm{div}\mathbf{V}\right)\mathrm{d}\Omega_e \tag{57}$$

$$\mathbf{k}'^{\mathrm{aux}}_{IJ} = \int_{\Omega_e} \left(\mathbf{B}_I^T\mathbf{D}^{\mathrm{aux}}\mathbf{B}'_J + \mathbf{B}_I^T\mathbf{D}^{\mathrm{aux}}\mathbf{B}'_J - \mathbf{B}_I^T\mathbf{D}^{\mathrm{aux}}\mathbf{B}_J\mathrm{div}\mathbf{V}\right)\mathrm{d}\Omega_e. \tag{58}$$

In Eqs. (57) and (58),

$$\mathbf{B}_I(\mathbf{x}) = \begin{bmatrix} \Phi_{I,1}(\mathbf{x}) & 0 \\ 0 & \Phi_{I,2}(\mathbf{x}) \\ \Phi_{I,2}(\mathbf{x}) & \Phi_{I,1}(\mathbf{x}) \end{bmatrix}, \tag{59}$$

$$\mathbf{B}'_I = \begin{bmatrix} \Phi_{I,1}(\mathbf{x})V_{1,1}(\mathbf{x}) + \Phi_{I,2}(\mathbf{x})V_{2,1}(\mathbf{x}) & 0 \\ 0 & \Phi_{I,1}(\mathbf{x})V_{1,2}(\mathbf{x}) + \Phi_{I,2}(\mathbf{x})V_{2,2}(\mathbf{x}) \\ \Phi_{I,1}(\mathbf{x})V_{1,2}(\mathbf{x}) + \Phi_{I,2}(\mathbf{x})V_{2,2}(\mathbf{x}) & \Phi_{I,1}(\mathbf{x})V_{1,1}(\mathbf{x}) + \Phi_{I,2}(\mathbf{x})V_{2,1}(\mathbf{x}) \end{bmatrix}, \tag{60}$$

and

$$\mathbf{D}'(\mathbf{x}) = \frac{\partial\mathbf{D}(\mathbf{x})}{\partial x_1}V_1(\mathbf{x}) + \frac{\partial\mathbf{D}(\mathbf{x})}{\partial x_2}V_2(\mathbf{x}), \tag{61}$$

with $\Phi_{I,i}(\mathbf{x})$ serving as the partial derivatives of the shape function corresponding to the Ith node in the i direction. Eq. (56) can be viewed as a discrete analog of the continuum formulation in Eq. (49). The former involves simple matrix algebra and, as a result, provides a convenient means for calculating $\tilde{M}^{(1,2)}$.

5.2 Velocity field

Defining the velocity field is an important step in any continuum shape sensitivity analysis [21]. For a fracture problem, the velocity field $\mathbf{V}(\mathbf{x})$ is defined with a compact support Ω_c, i.e., $\mathbf{V}(\mathbf{x})$, is non-zero when $\mathbf{x} \in \Omega_c$ and is zero when $\mathbf{x} \in \Omega - \Omega_c$, where $\Omega_c \subset \Omega$ is an appropriately small subdomain around the crack tip (see Fig. 1). Hence, the domain Ω in various integrals (see Eqs. (50)–(51)) can be replaced by the subdomain Ω_c. Specifically, consider a rosette of eight 6-noded quarter-point elements around a crack tip, as shown in Fig. 3. These quarter-point elements are standard finite elements commonly employed for fracture analysis of linear-elastic bodies. Assume that the size of these elements is small enough that the rosette can be defined as support Ω_c. Inside Ω_c, the velocity field satisfies the following conditions: (1) the crack tip is assigned a velocity of unit magnitude, *i.e.*, $\mathbf{V}(\mathbf{0}) = \left(\mathbf{1}\Big/\sqrt{\mathbf{V}_{\mathbf{1},\mathrm{tip}}^2 + \mathbf{V}_{\mathbf{2},\mathrm{tip}}^2}\right)\left\{\mathbf{V}_{\mathbf{1},\mathrm{tip}}, \mathbf{V}_{\mathbf{2},\mathrm{tip}}\right\}^{\mathrm{T}}$; (2) the velocity at a point on the boundary Γ_c of the rosette is zero; and (3) velocity at any point between boundary Γ_c and the crack tip varies linearly. For example, the velocity $\mathbf{V}(\mathbf{x}_i)$ at the ith node of the quarter-point elements in Fig. 3 can be defined as

$$\mathbf{V}(\mathbf{x}_i) = \begin{cases} \mathbf{0}, & \text{if } i \text{ is a node on the outer ring (open circles)} \\ 0.75\mathbf{V}(\mathbf{0}), & \text{if } i \text{ is a quarter-point node (closed circles)} \\ \mathbf{V}(\mathbf{0}), & \text{if } i \text{ is the crack-tip node (closed circle)} \end{cases} \tag{62}$$

Since the velocity field is zero on and outside the outer boundary of the quarter point elements, Eq. (56) reduces to

$$\tilde{M}^{(1,2)} \cong \sum_{I,J=1}^{M} \mathbf{z}_I^{(1)T}\mathbf{K}'_{IJ}\mathbf{z}_J^{(2)} + \frac{1}{2}\sum_{I,J=1}^{M} \mathbf{z}_I^{(2)T}\left(\mathbf{K}'_{IJ} - \mathbf{K}'^{\mathrm{aux}}_{IJ}\right)\mathbf{z}_J^{(2)}, \tag{63}$$

where M is the total number of quarter-point and crack tip nodes in a rosette of focused quarter-point elements near the crack tip, as shown by the closed circles in Fig. 3. In other words, displacement response is only required at an M number of nodes. Since $M \ll N$, the effort in computing $\tilde{M}^{(1,2)}$

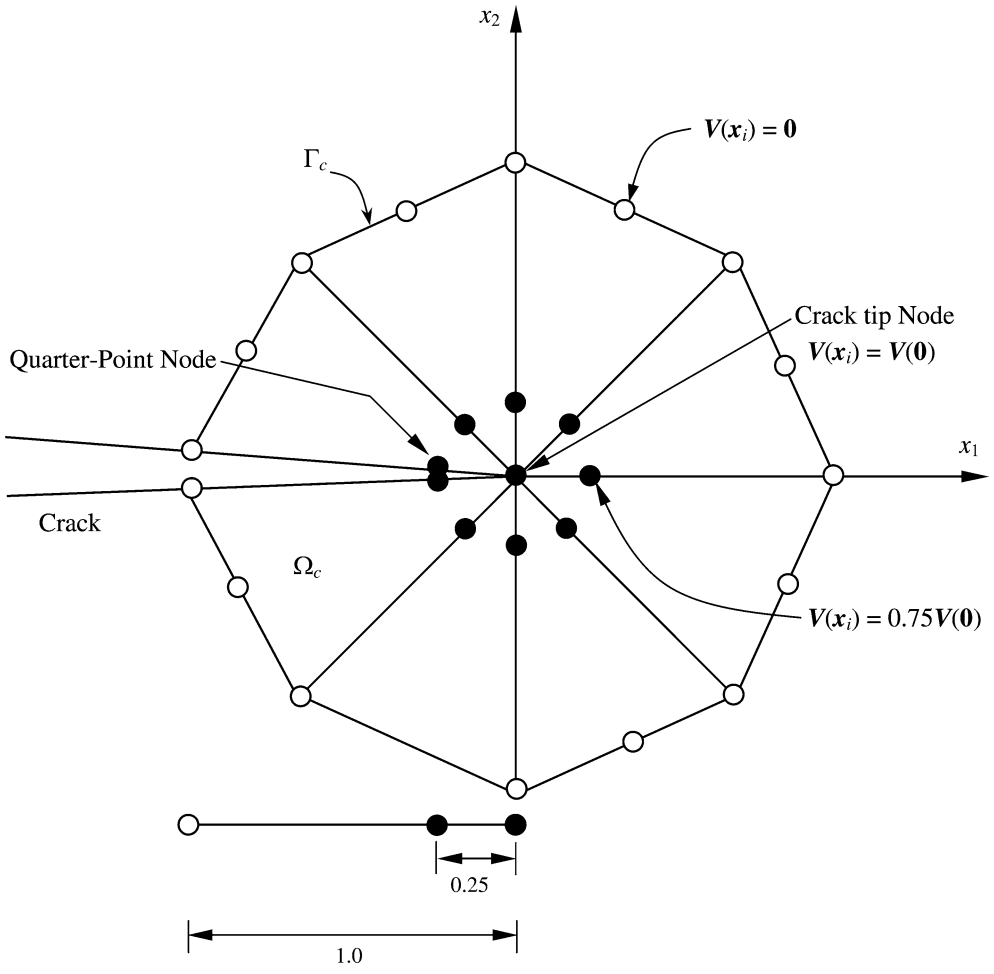

Fig. 3 Rosette of focused quarter-point 6-noded triangular elements near the crack tip

using Eq. (63) is trivial compared to that required for a complete stress analysis.

Compared with existing methods, the proposed method has several advantages: (1) the calculation of SIFs is simple and straightforward as it only requires multiplication of displacement vectors and stiffness sensitivity matrices; (2) since Ω_c is small and the velocity field outside Ω_c is zero, the method only requires displacement response in Ω_c, rendering it computationally efficient; (3) the accuracy of SIF estimates is not affected by a lack of smooth transition between mesh resolutions inside and outside Ω_c, as demonstrated by numerical results; and (4) the method is applicable to multiple interacting cracks even if crack tips are close to one other.

Unlike in the displacement correlation method, and the modified crack-closure integral method SIFs are calculated in the proposed method using displacement response around the crack tip in an average sense. When compared with existing integral based methods such as the J-integral, the J_k^*-integral, and the interaction integral the proposed method requires displacement response only in a small portion around the crack tip. In addition, in case of multiple interacting cracks with crack tips very close to one other, it is very difficult to choose a domain around the crack tip with size enough for accurate evaluation of SIFs using existing integral based methods and hence, the proposed method provides an alternative in such cases. Also, in contrast to existing methods, such as the J_k^* -integral method [3], there is no need to perform integration along the crack face of the discontinuity (e.g., in calculating J_2^*). Hence, the proposed method is also simpler and more efficient than existing methods.

6 Numerical examples

In conjunction with the newly developed shape sensitivity method, standard FEM was applied to evaluate the SIFs of rectilinear cracks in two-dimensional FGM structures. Both single- (mode I) and mixed-mode (modes I and II) conditions were considered and seven examples are presented here. In all seven examples, the elastic modulus varies spatially, while the Poisson's ratio ν is held constant. This is a reasonable assumption, since variation of the Poisson's ratio is usually small compared with that of the elastic modulus. In examples 1–6 Poisson's ratio ν was assumed to be 0.3 and whereas in example 7 it was taken to be 0.0. For numerical integration, a 2×2 Gauss quadrature rule was used in all examples.

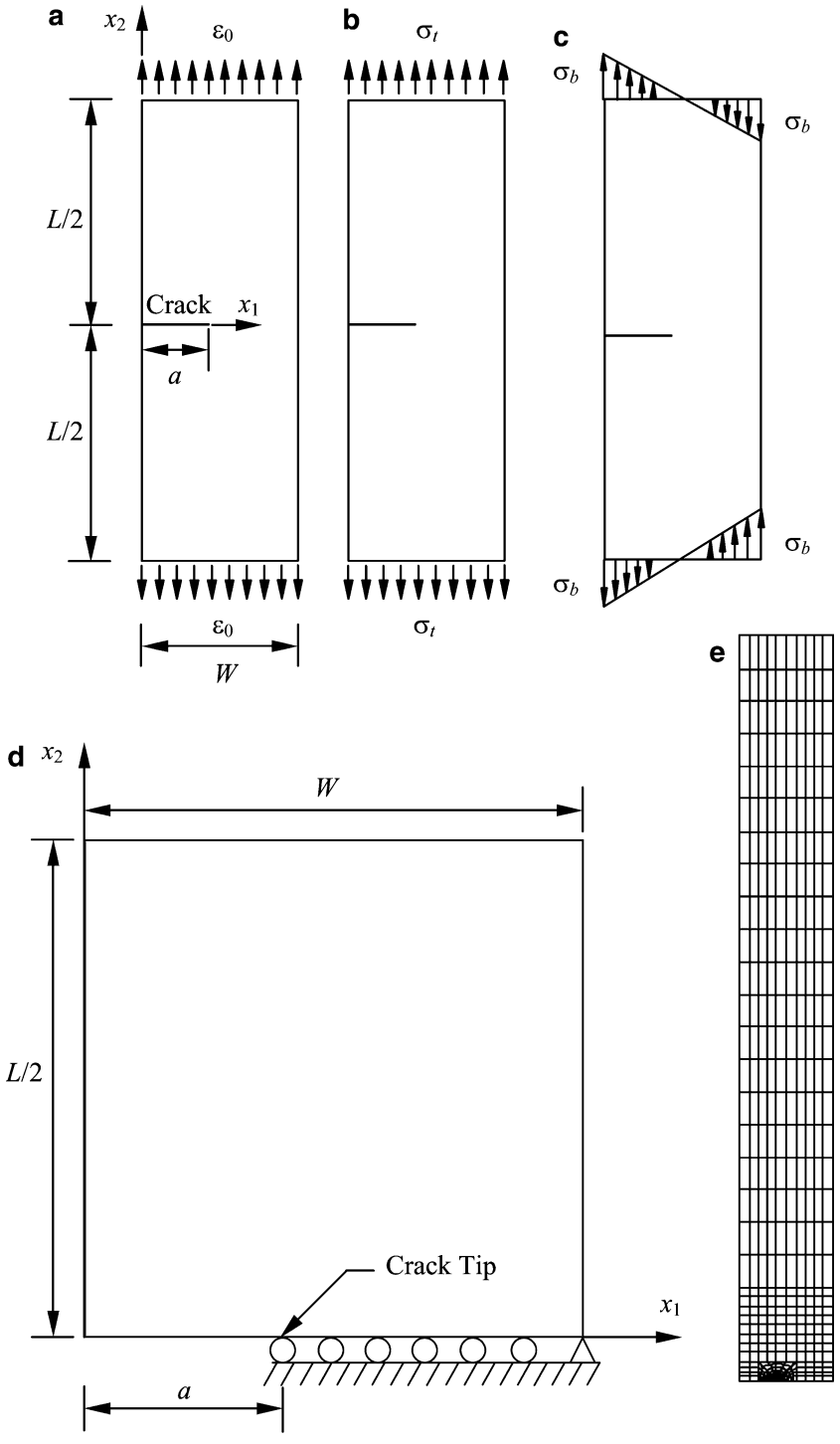

Fig. 4 Edge-cracked plate under mode I loading; (a) Geometry and loads for fixed grip loading; (b) Membrane loading; (c) Bending; (d) Half model; and (e) FEM discretization of half model for $a/W = 0.4$

6.1 Example 1: Edge-cracked plate under mode-I

Consider an edge-cracked plate with length $L = 8$ units, width $W = 1$ unit, and crack length a, as shown in Fig. 4a. Three loading conditions including the uniform fixed grip loading (constant strain), the membrane loading (constant tensile stress), and pure bending (linear stress) were considered. Figs. 4a–c show the schematics of the three loading conditions. The elastic modulus was assumed to follow an exponential function, given by

$$E(x_1) = E_1 \exp(\eta x_1), \quad 0 \le x_1 \le W \tag{64}$$

where $E_1 = E(0)$, $E_2 = E(W)$, and $\eta = \ln\left(E_2/E_1\right)$. In Eq. (64), E_1 and η are two independent material parameters that characterize the elastic modulus variation. The following numerical values were used: $E_1 = 1$ unit, $E_2/E_1 = \exp(\eta) = 0.1, 0.2, 5,$ and 10, and $a/W = 0.2, 0.3, 0.4, 0.5$ and 0.6. A plane strain condition was assumed. Erdogan and Wu [22], who originally studied this example, also provided a theoretical solution.

Due to the symmetry of geometry and load, only half of the plate, as shown in Fig. 4d, was analyzed by FEM. Fig. 4e shows typical FEM discretization involving 1285 nodes, 388 8-noded quadrilateral (Q8) elements, and 12 focused quarter-point 6-noded triangular (T6) elements, adopted for $a/W = 0.4$. A crack tip velocity $\left\{V_{1,\text{tip}}, V_{2,\text{tip}}\right\}^{\text{T}} = \left\{10^{-5}a, 0\right\}^{\text{T}}$ was used in the analysis.

Tables 1–3 show normalized mode-I stress intensity factors $K_I/\sigma_0\sqrt{\pi a}$, $K_I/\sigma_t\sqrt{\pi a}$, and $K_I/\sigma_b\sqrt{\pi a}$ for fixed grip, membrane loading, and bending, respectively, where $\sigma_0 = E_1\varepsilon_0/\left(1-\nu^2\right)$, $\varepsilon_0 = 1$, $\sigma_t = \sigma_b = 1$ unit. The results show that the predicted SIF obtained by the proposed method agrees very well with the analytical results of Erdogan and Wu [22], for all three types of loading and for various combinations of E_2/E_1 and a/W ratios. In addition, Tables 1–3 include some numerical results by Kim and Paulino [23] and/or Chen et al. [24]. The present results correlate satisfactorily with the FEM results of Kim and Paulino based on J_1^*-integral, which are only reported for membrane loading and bending. The mesh-free results of Chen et al., which are reported for fixed grip and membrane loading, also agree reasonably well with the present results. It is worth noting that the mesh-free results of Chen et al. are based on the classical J-integral for homogenous materials.

6.2 Example 2: Three-point bend specimen under mode-I

Consider a three-point bend specimen with length $L = 54$ units, depth $2H = 10$ units, and thickness $t = 1$ unit, as shown in Fig. 5a. A concentrated load of $P = 1$ unit was applied at the middle of the beam of span $L_S = 50$ units and two supports were symmetrically placed with respect to an edge crack of length a. In the depth direction, the beam consists of $2h$ units deep FGM sandwiched between two distinct homogeneous materials, each of which has depth $H-h$. If E_1 and E_2 represent the elastic moduli of the bottom and top layers, the elastic modulus of the FGM layer varies linearly, with the end values matching the properties of the bottom and top layers. Mathematically, such a variation can be defined as

$$E(x_1) = \begin{cases} E_2, & x_1 \geq h \\ \frac{E_1+E_2}{2} + \frac{E_2-E_1}{2h}x_1, & -h \leq x_1 \leq h \\ E_1, & x_1 \leq -h \end{cases}, \tag{65}$$

where E_1, E_2, and $2h$ are material/geometry parameters. The following numerical values were chosen: $2h = 1$ unit, $E_1 = 1$ unit, and $E_2/E_1 = 0.05, 0.1, 0.2, 0.5, 1, 2, 5, 10,$ and 20. For each E_2/E_1 ratio, three different crack lengths with $a/2H = 0.45$, 0.5 and 0.55 were selected such that the crack tips were either at the middle of the FGM layer ($a/2H = 0.5$) or at the material interfaces ($a/2H = 0.45$ or 0.55). A plane stress condition was assumed.

Due to symmetric geometry and loading with respect to the crack, only a half model of the beam was analyzed, as shown in Fig. 5b. Figure 5c shows typical FEM discretization involving 2053 nodes, 640 Q8 elements, and 12 focused quarter-point T6 elements, adopted for $a/2H = 0.5$. A crack tip velocity $\left\{V_{1,\text{tip}}, V_{2,\text{tip}}\right\}^{\text{T}} = \left\{10^{-5}a, 0\right\}^{\text{T}}$ was employed.

Table 4 shows the predicted normalized mode-I SIF $K_I\sqrt{H}/P$, obtained by the proposed method for various combinations of E_2/E_1 and $a/2H$. Also presented in Table 4 are the corresponding results by Kim and Paulino [23]. The SIFs by the proposed method are in good agreement with the results by Kim and Paulino based on J_1^*-integral. Although not presented here, the graphical results of Gu *et al*. [25] also agree well with the present results.

6.3 Example 3: Edge-cracked plate under mixed-mode loading

This mixed-mode example involves the edge-cracked plate in Fig. 6a, which is fixed at the bottom and subjected to a far-field shear stress $\tau^{\infty} = 1$ unit applied on the top. The plate has length $L = 16$ units, width $W = 7$ units, and crack length $a = 3.5$ units. The elastic modulus was assumed to follow an exponential function, given by

$$E(x_1) = E_1 \exp\left(\frac{\eta x_1}{W}\right), \quad 0 \leq x_1 \leq W \tag{66}$$

where $E_1 = E(0)$, $E_2 = E(W)$, and $\eta = \ln\left(E_2/E_1\right)$. In Eq. (66), E_1 and η are two independent material parameters that characterize the elastic modulus variation. The following numerical values were used: $E_1 = 1$ unit, $E_2/E_1 = \exp(\eta) = 0.1, 0.2, 5,$ and 10, and $a/W = 0.2, 0.3, 0.4, 0.5$ and 0.6. A plane strain condition was assumed. Figure 6b shows FEM discretization involving 2711 nodes, 832 Q8 elements, and 48 focused quarter-point T6 elements, adopted to solve with the proposed method. A velocity field $\left\{V_{1,\text{tip}}, V_{2,\text{tip}}\right\}^{\text{T}} = \left\{10^{-5}a, 0\right\}^{\text{T}}$ was used in the analysis.

Recently, Rao and Rahman [4] also solved this problem using two interaction integrals, referred to as Method-I and Method-II. However, the auxiliary fields employed in [4] are different from the one defined in the present study. It would be interesting to compare the results of the present method with those of Methods-I and II [4]. Table 5 shows the predicted mixed-mode SIFs for this edge-cracked problem, obtained in the present study for various values of E_2/E_1 using the proposed method. Table 5 also shows the predicted mixed-mode SIFs, obtained for various values of E_2/E_1 using Method-I and Method-II [4]. The results in Table 5 demonstrate that the present method using continuum shape sensitivity provides accurate estimates of K_I and K_{II} as compared with

Table 1 Normalized mode-I stress intensity factor for an edge-cracked plate under fixed grip loading

Method	E_2/E_1	$K_I/\sigma_0\sqrt{\pi a}$				
		$a/W = 0.2$	$a/W = 0.3$	$a/W = 0.4$	$a/W = 0.5$	$a/W = 0.6$
Present method	0.1	1.3018	1.5102	1.8161	2.2763	3.0225
	0.2	1.3117	1.5376	1.8758	2.3922	3.2398
	5	1.4918	1.9089	2.5701	3.6545	5.5685
	10	1.5681	2.0656	2.8654	4.2033	6.6158
Erdogan and Wu [22]	0.1	1.2963	1.5083	1.8246	2.3140	3.1544
	0.2	1.3058	1.5330	1.8751	2.4031	3.2981
	5	1.4946	1.9118	2.5730	3.6573	5.5704
	10	1.5740	2.0723	2.8736	4.2140	6.6319
Chen et al. [24]	0.1	1.2961	1.4919	1.7962	2.2594	3.0544
	0.2	1.3145	1.5283	1.8659	2.3877	3.2910
	5	1.5414	1.9499	2.6238	3.7429	5.7936
	10	1.6296	2.1206	2.9398	4.3272	6.9171

Table 2 Normalized mode-I stress intensity factor for an edge-cracked plate under membrane loading

Method	E_2/E_1	$K_I/\sigma_t\sqrt{\pi a}$				
		$a/W = 0.2$	$a/W = 0.3$	$a/W = 0.4$	$a/W = 0.5$	$a/W = 0.6$
Present method	0.1	1.3053	1.8647	2.5653	3.5260	5.0000
	0.2	1.4028	1.8462	2.4466	3.3153	4.6983
	5	1.1285	1.3666	1.7453	2.3629	3.4435
	10	0.9958	1.2229	1.5819	2.1687	3.2026
Erdogan and Wu [22]	0.1	1.2965	1.8581	2.5699	3.5701	5.1880
	0.2	1.3956	1.8395	2.4436	3.3266	4.7614
	5	1.1318	1.3697	1.7483	2.3656	3.4454
	10	1.0019	1.2291	1.5884	2.1762	3.2124
Chen et al. [24]	0.1	1.3193	1.8642	2.5588	3.5213	5.0726
	0.2	1.4188	1.8497	2.4486	3.3234	4.7860
	5	1.1622	1.3899	1.7746	2.4125	3.5736
	10	1.0324	1.2499	1.6146	2.2234	3.3371
Kim and Paulino [23] (J_1^*)	0.1	1.2840	1.8460	2.5440	3.4960	4.9620
	0.2	1.3900	1.8310	2.4310	3.2920	4.6690
	5	1.1320	1.3700	1.7490	2.3660	3.4480
	10	1.0030	1.2280	1.5880	2.1750	3.2120

Table 3 Normalized mode-I stress intensity factor for an edge-cracked plate under bending

Method	E_2/E_1	$K_I/\sigma_b\sqrt{\pi a}$				
		$a/W = 0.2$	$a/W = 0.3$	$a/W = 0.4$	$a/W = 0.5$	$a/W = 0.6$
Present method	0.1	1.9075	1.8831	1.9606	2.1649	2.5750
	0.2	1.6007	1.6153	1.7188	1.9392	2.3568
	5	0.6835	0.7747	0.9208	1.1557	1.5578
	10	0.5589	0.6533	0.7990	1.0296	1.4224
Erdogan and Wu [22]	0.1	1.9040	1.8859	1.9778	2.2151	2.7170
	0.2	1.5952	1.6122	1.7210	1.9534	2.4037
	5	0.6871	0.7778	0.9236	1.1518	1.5597
	10	0.5648	0.6588	0.8043	1.0350	1.4286
Kim and Paulino [23] (J_1^*)	0.1	1.8880	1.8640	1.9430	2.1450	2.5530
	0.2	1.5880	1.6010	1.7060	1.9250	2.3410
	5	0.6870	0.7780	0.9240	1.1580	1.5610
	10	0.5650	0.6590	0.8040	1.0350	1.4290

corresponding results obtained using previously developed methods.

Convergence of the results with mesh refinement around the crack tip is studied by varying the number of square rings around the crack tip. The following four mesh refinements were used: (1) 2565 nodes, 784 Q8 elements, and 48 focused quarter-point T6 elements; (2) 2711 nodes, 832 Q8 elements, and 48 focused quarter-point T6 elements; (3) 2857 nodes, 880 Q8 elements, and 48 focused quarter-point T6 elements; and (4) 3003 nodes, 928 Q8 elements, and 48 focused

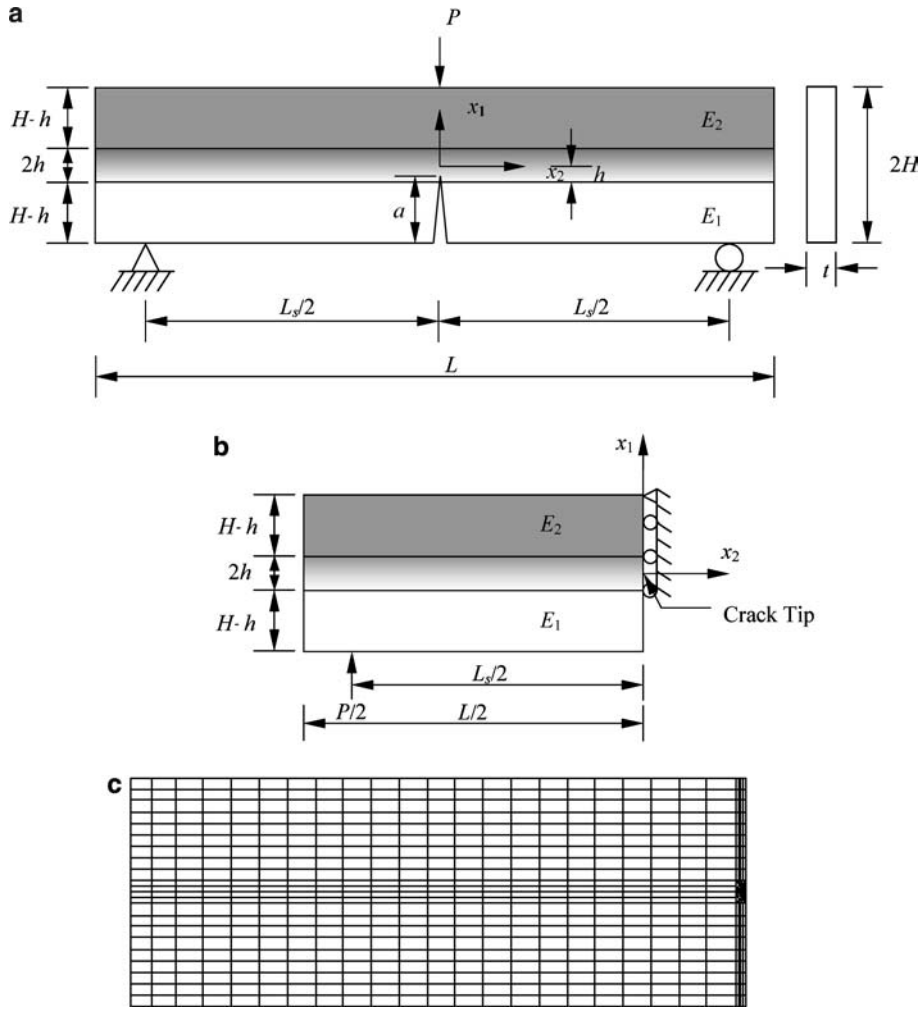

Fig. 5 Three-point bend specimen under mode I loading; (a) Geometry and loads; (b) Half model; and (c) FEM discretization of half model for $a/2H = 0.5$

Table 4 Normalized mode-I stress intensity factor for a three-point bend specimen

E_2/E_1	$K_I\sqrt{H}/P$ $(a/2H = 0.45)$		$K_I\sqrt{H}/P$ $(a/2H = 0.5)$		$K_I\sqrt{H}/P$ $(a/2H = 0.55)$	
	Present method	Kim and Paulino [23] (J_1^*)	Present method	Kim and Paulino [23] (J_1^*)	Present method	Kim and Paulino [23] (J_1^*)
0.05	33.1600	33.04	31.6520	31.12	16.2605	15.21
0.1	23.5562	23.47	24.1546	23.92	14.3199	13.73
0.2	17.4201	17.36	18.4720	18.32	13.0044	12.79
0.5	11.6899	11.65	12.6464	12.57	11.8318	11.76
1	8.1585	8.134	9.4868	9.467	11.1826	11.15
2	5.2318	5.239	7.3024	7.318	10.6301	10.62
5	2.5010	2.540	5.4596	5.496	9.9625	9.963
10	1.2650	1.334	4.5519	4.586	9.5032	9.505
20	0.5505	0.660	3.9202	3.939	9.1194	9.123

quarter-point T6 elements. Convergence of normalized mode-I and mode-II stress intensity factors with mesh refinement was observed as shown in Fig. 7a,b.

6.4 Example 4: Slanted crack in a plate under mixed-mode

Consider a slanted crack in a finite two-dimensional plate with length $L = 2$ units, width $W = 1$ unit and a 45-degree edge crack of normalized length $a/W = 0.4\sqrt{2}$, as shown in Fig. 8a. The elastic modulus was assumed to follow an exponential function, given by

$$E(x_1) = \bar{E}\exp\left[\eta\left(x_1 - \frac{1}{2}\right)\right], \quad 0 \le x_1 \le W, \tag{67}$$

where $\bar{E}$ and η are two material parameters. For numerical values, $\bar{E} = 1$ unit and $\eta = 0, 0.1, 0.25, 0.5, 0.75,$ and 1.

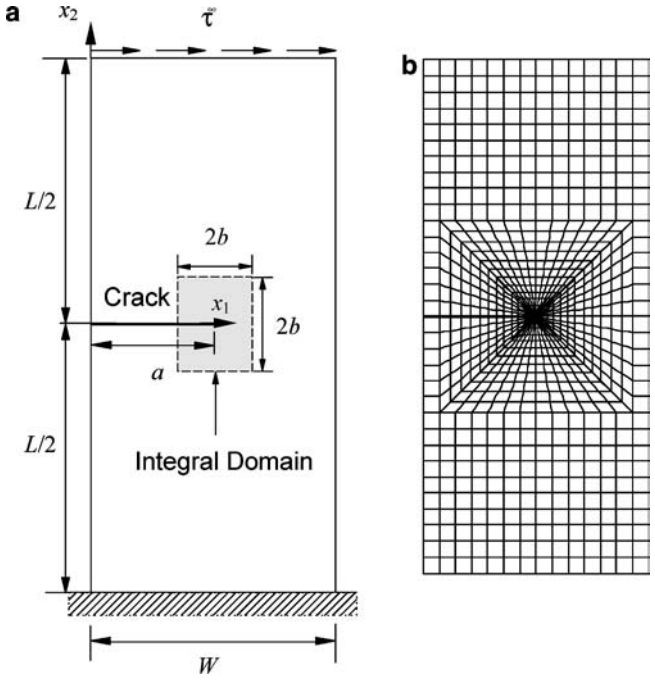

Fig. 6 Edge-cracked plate under mixed-mode loading; (a) Geometry, loads, and domain size; and (b) FEM discretization

A plane stress condition was assumed. The applied load was prescribed along the upper edge with normal stress $\sigma_{22}(x_1, 1) = \bar{\varepsilon}\bar{E}\exp[\eta(x_1 - 0.5)]$, where $\bar{\varepsilon} = 1$. The displacement boundary condition was specified such that $u_2 = 0$ along the lower edge and, in addition, $u_1 = 0$ for the node on the right side of the lower edge. FEM discretization involved 1541 nodes, 460 Q8 elements, and 40 focused quarter-point T6 elements, as shown in Fig. 8b. A crack tip velocity $\{V_{1,\text{tip}}, V_{2,\text{tip}}\}^{\text{T}} = \{10^{-5}a\cos\gamma,\ 10^{-5}a\sin\gamma\}^{\text{T}}$ was used in the analysis. Using the same FEM discretization, the current example was also solved using Methods-I and II by Rao and Rahman [4], as described in the previous example.

Table 6 shows the predicted normalized SIFs $K_I/\bar{\varepsilon}\bar{E}\sqrt{\pi a}$ and $K_{II}/\bar{\varepsilon}\bar{E}\sqrt{\pi a}$, obtained in the present study for several values of η using the proposed method. Table 6 also shows the predicted normalized SIFs obtained by using Methods-I and II [4] as well as Kim and Paulino's [23] results for various values of η. The results in Table 6 demonstrate that the present method using continuum shape sensitivity provides accurate estimates of K_I and K_{II} as compared with the corresponding results of Rao and Rahman [4] based interaction integral and Kim and Paulino [23] based on J_1^*-integral. Agreement between the proposed method and reference solutions is excellent.

Table 5 Stress intensity factors for an edge cracked plate under shear loading

E_2/E_1	Present method		Method-I [4]		Method-II [4]	
	K_I	K_{II}	K_I	K_{II}	K_I	K_{II}
0.1	49.2461	5.9854	48.8532	6.1650	48.8376	6.1714
0.2	44.0892	5.5538	43.8357	5.6606	43.8260	5.6646
1	34.0791	4.5911	34.0624	4.5898	34.0624	4.5898
5	26.2487	3.7048	26.3785	3.6372	26.3839	3.6352
10	23.3918	3.3454	23.5638	3.2532	23.5705	3.2509

6.5 Example 5: Composite strip under mode I

For this example, consider the square composite strip configuration studied by Eischen [19] with size $L = 1$ unit, $2h_1 = 0.6$ units and $2h_2 = 0.4$ units, as shown in Fig. 9a. A crack of length $a = 0.4$ units is located on the line $x_2 = 0$. The elastic modulus was assumed to vary smoothly according to a hyperbolic-tangent function, given by

$$E(x_1) = \frac{E_1 + E_2}{2} + \frac{E_1 - E_2}{2}\tanh[\eta(x_1 + 0.1)], \quad -0.5 \le x_1 \le 0.5, \tag{68}$$

where E_1 and E_2 are the bounds of $E(x_1)$, and η is a non-homogeneity parameter that controls the variation of $E(x_1)$ from E_1 to E_2, as shown in Fig. 9a. When $\eta \to \infty$, a sharp discontinuity occurs in the slope of $E(x_1)$ across the interface at $x_1 = -0.1$. A tensile load corresponding to $\sigma_{22}(x_1, 1) = \bar{\varepsilon}E(x_1)/(1-\nu^2)$ was applied at the top edge, which results in a uniform strain $\varepsilon_{22}(x_1, x_2) = \bar{\varepsilon}$ in the corresponding uncracked structure. The following numerical values were used: $E_1 = 1$ unit, $E_2 = 3$ units, $\eta a = 0, 2, 4, 6,$ and 20 units, and $\bar{\varepsilon} = 1$. A plane strain condition was assumed. FEM discretization involved 823 nodes, 244 Q8 elements, and 16 focused quarter-point T6 elements, as shown in Fig. 9b. A crack tip velocity $\{V_{1,\text{tip}}, V_{2,\text{tip}}\}^{\text{T}} = \{10^{-5}a, 0\}^{\text{T}}$ was employed.

Table 7 compares the predicted normalized mode-I SIF $K_I/[\bar{\varepsilon}E(-0.5)\sqrt{\pi a}]$ obtained in the present study with Eischen's results based on J_k^*-integral for several values of ηa. The normalized SIF results obtained in the present study agree very well with the reference solution.

6.6 Example 6: Plate with an interior inclined crack under mixed-mode

Consider a centrally located inclined crack of length $2a = 2$ units and an orientation γ in a finite, two-dimensional square plate of size $2L = 2W = 20$ units, as shown in Fig. 10a. Plane stress conditions were assumed. The elastic modulus was assumed to be an exponential function, given by

$$E(x_1) = \bar{E}\exp(\eta x_1), \quad -W \le x_1 \le W, \tag{69}$$

where $\bar{E}$ and η are material parameters. The following data were used for the numerical study: $\bar{E} = 1$ unit; $\eta = 0.25$ and 0.5; and $\gamma/\pi = 0, 0.1, 0.2, 0.3, 0.4,$ and 0.5. The applied load corresponds to $\sigma_{22}(x_1, 10) = \bar{\varepsilon}\bar{E}\exp(\eta x_1)$, where $\bar{\varepsilon} = 1$. This stress distribution was obtained by applying nodal forces along the top edge of the plate. The displacement boundary condition was prescribed such that $u_2 = 0$ along the lower edge and, in addition, $u_1 = 0$ for the node on the left hand

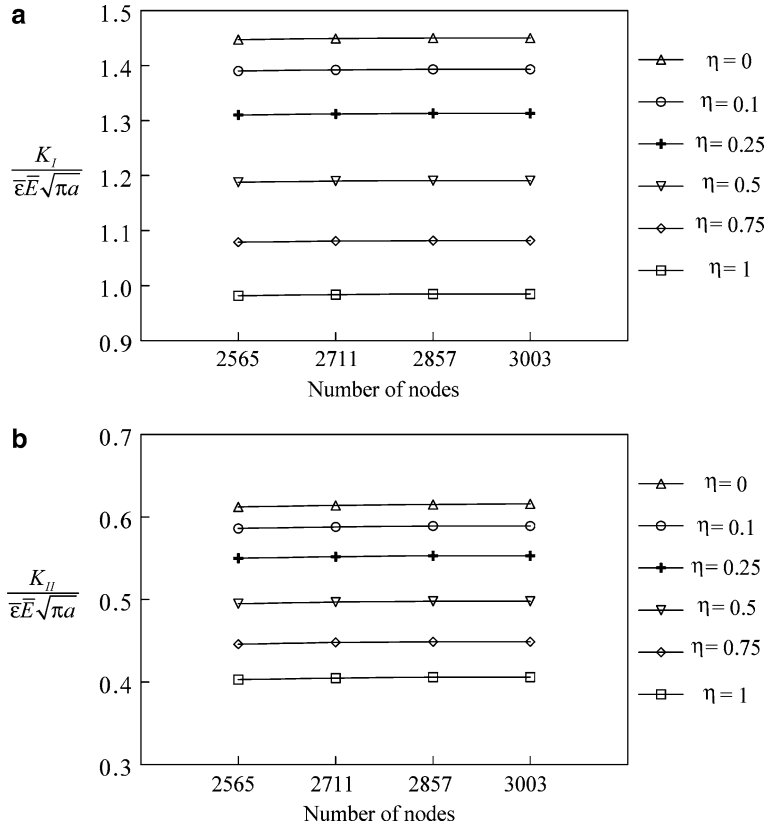

Fig. 7 Convergence of results with mesh refinement near the crack tip; (a) Normalized mode-I stress intensity factor and (b) Normalized mode-II stress intensity factor

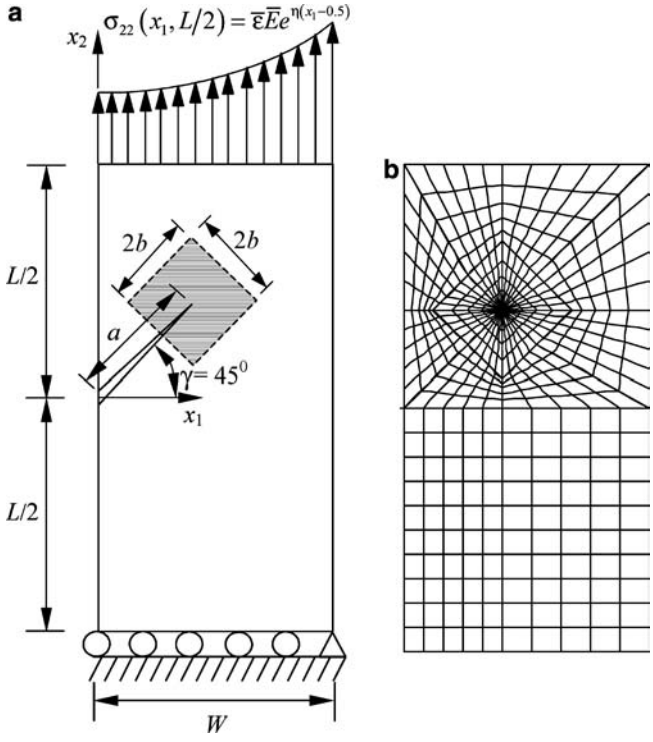

Fig. 8 Slanted Crack in a plate under mixed mode loading; (a) Geometry and loads; and (b) FEM discretization

side of the lower edge. This loading results in a uniform strain $\varepsilon_{22}(x_1, x_2) = \bar{\varepsilon}$ in a corresponding uncracked structure. Figure 10b shows typical FEM discretization involving 2092 nodes, 628 Q8 elements, and 68 focused quarter-point T6 elements, adopted for $\gamma/\pi = 0.2$. In the analysis, a velocity $\left\{V_{1,\text{tip}}, V_{2,\text{tip}}\right\}^{\text{T}} = \left\{10^{-5}a\cos\gamma, -10^{-5}a\sin\gamma\right\}^{\text{T}}$ was used at the right crack tip, while a velocity $\left\{V_{1,\text{tip}}, V_{2,\text{tip}}\right\}^{\text{T}} = \left\{-10^{-5}a\cos\gamma,\ 10^{-5}a\sin\gamma\right\}^{\text{T}}$ was used at the left crack tip.

Konda and Erdogan [26] previously investigated an infinite plate with a similar configuration. Although an FEM model cannot represent the infinite domains addressed in their analysis, as long as the ratios a/W and a/L are kept relatively small (e.g., $a/W = a/L \leq 1/10$), the approximation is acceptable. Tables 8 and 9 provide a comparison between the predicted normalized SIFs for both crack tips, $K_I(+a)/\bar{E}\bar{\varepsilon}\sqrt{\pi a}$, $K_I(-a)/\bar{E}\bar{\varepsilon}\sqrt{\pi a}$, $K_{II}(+a)/\bar{E}\bar{\varepsilon}\sqrt{\pi a}$, and $K_{II}(-a)/\bar{E}\bar{\varepsilon}\sqrt{\pi a}$, obtained by the proposed method and those of Konda and Erdogan [28] for several values of γ/π, when $\eta = 0.25$ and $\eta = 0.5$, respectively. A good agreement is obtained between present FEM results and Konda and Erdogan's analytical solution.

Table 6 Normalized stress intensity factors for a slanted crack in a plate

η	Present method		Method-I [4]		Method-II [4]		Kim and Paulino [23] (J_k^*)	
	$\frac{K_I}{\bar{\varepsilon}\bar{E}\sqrt{\pi a}}$	$\frac{K_{II}}{\bar{\varepsilon}\bar{E}\sqrt{\pi a}}$	$\frac{K_I}{\bar{\varepsilon}\bar{E}\sqrt{\pi a}}$	$\frac{K_{II}}{\bar{\varepsilon}\bar{E}\sqrt{\pi a}}$	$\frac{K_I}{\bar{\varepsilon}\bar{E}\sqrt{\pi a}}$	$\frac{K_{II}}{\bar{\varepsilon}\bar{E}\sqrt{\pi a}}$	$\frac{K_I}{\bar{\varepsilon}\bar{E}\sqrt{\pi a}}$	$\frac{K_{II}}{\bar{\varepsilon}\bar{E}\sqrt{\pi a}}$
0	1.449	0.614	1.448	0.610	1.448	0.610	1.451	0.604
0.1	1.392	0.588	1.392	0.585	1.391	0.585	1.396	0.579
0.25	1.312	0.552	1.313	0.549	1.312	0.549	1.316	0.544
0.5	1.190	0.497	1.193	0.495	1.190	0.495	1.196	0.491
0.75	1.081	0.448	1.086	0.447	1.082	0.446	1.089	0.443
1	0.984	0.405	0.990	0.405	0.986	0.404	0.993	0.402

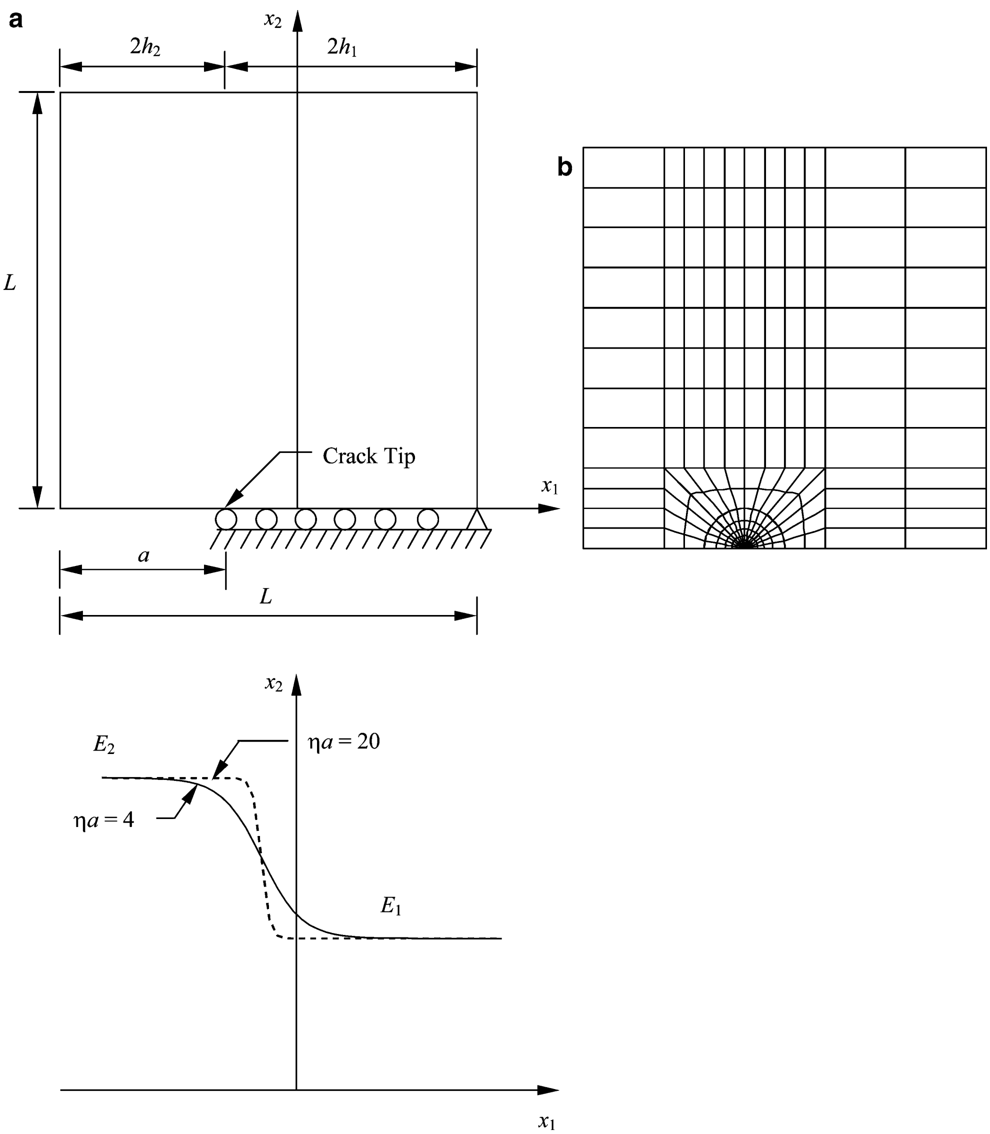

Fig. 9 Composite strip under mode-I loading; (a) Geometry and Elastic modulus variation; (b) FEM discretization

6.7 Example 7: Plate with two interacting cracks under mixed-mode loading

Consider a finite two-dimensional square plate of size $2L = 2W = 20$ units, containing two cracks of length $2a = 2$ units, oriented with angles $\theta_1 = 30^0$, $\theta_2 = 60^0$, as shown in Fig. 11a. The distance from the origin to each of the two left crack tips is 1.0 unit. Plane stress conditions were assumed. The elastic modulus was assumed to be an exponential function of x_2, given by

$$E\left(x_2\right) = \bar{E}\exp\left(\beta x_2\right), \quad -L \le x_2 \le L, \tag{70}$$

Table 7 Normalized mode-I stress intensity factor for a composite strip configuration

$\eta\, a$	$\frac{K_I}{\bar{\varepsilon} E\,(-0.5)\,\sqrt{\pi a}}$	
	Proposed method	Eischen [19]
0	2.1159	2.112
2	2.3027	2.295
4	2.5821	2.571
6	2.7473	2.733
20	3.2485	3.228

where $\bar{E}$ and β are material parameters. The following data were used for the numerical study: $\bar{E} = 1$ unit; and $\beta\, a$ = 0.0, 0.25, 0.5, 0.75, and 1.0. The applied load corresponds to $\sigma_{22}\,(x_1, 10) = \sigma_0 = 1.0$. This stress distribution was obtained by applying nodal forces along the top edge of the mesh. The displacement boundary condition was prescribed such that $u_2 = 0$ along the lower edge and, in addition, $u_1 = 0$ for the node on the left hand side of the lower edge. FEM discretization involved 3093 nodes, 936 Q8 elements, and 64 focused quarter-point T6 elements, as shown in Fig. 11b. Velocities $\left\{V_{1,\text{tip}},\, V_{2,\text{tip}}\right\}^{\text{T}} = \left\{10^{-5}a\cos\theta_1,\, 10^{-5}a\sin\theta_1\right\}^{\text{T}}$ and $\left\{V_{1,\text{tip}},\, V_{2,\text{tip}}\right\}^{\text{T}} = \left\{-10^{-5}a\cos\theta_1,\, -10^{-5}a\sin\theta_1\right\}^{\text{T}}$ were employed at right and left crack tips, respectively, of the lower crack.

Kim and Paulino [23] investigated this example using the displacement correlation technique, the modified crack-closure integral method and the J_k^* integral method. In addition, Shbeeb et al. [27,28] provided semi-analytical solutions obtained using an integral equation method. However, the results of Shbeeb et al. were only presented in graphical form, making accurate verification difficult. Nevertheless, Table 10 provides a comparison between the predicted normalized SIFs, $K_I(+a)\big/\sigma_{22}\sqrt{\pi a}$, $K_{II}(+a)\big/\sigma_{22}\sqrt{\pi a}$, $K_I(-a)\big/\sigma_{22}\sqrt{\pi a}$, and $K_{II}(-a)\big/\sigma_{22}\sqrt{\pi a}$, for both crack tips of the lower crack obtained by the proposed method and those of Kim and Paulino and Shbeeb et al. for several values of $\beta\, a$. A good agreement is obtained between the present FEM results and published solutions of both Kim and Paulino and Shbeeb *et al.*

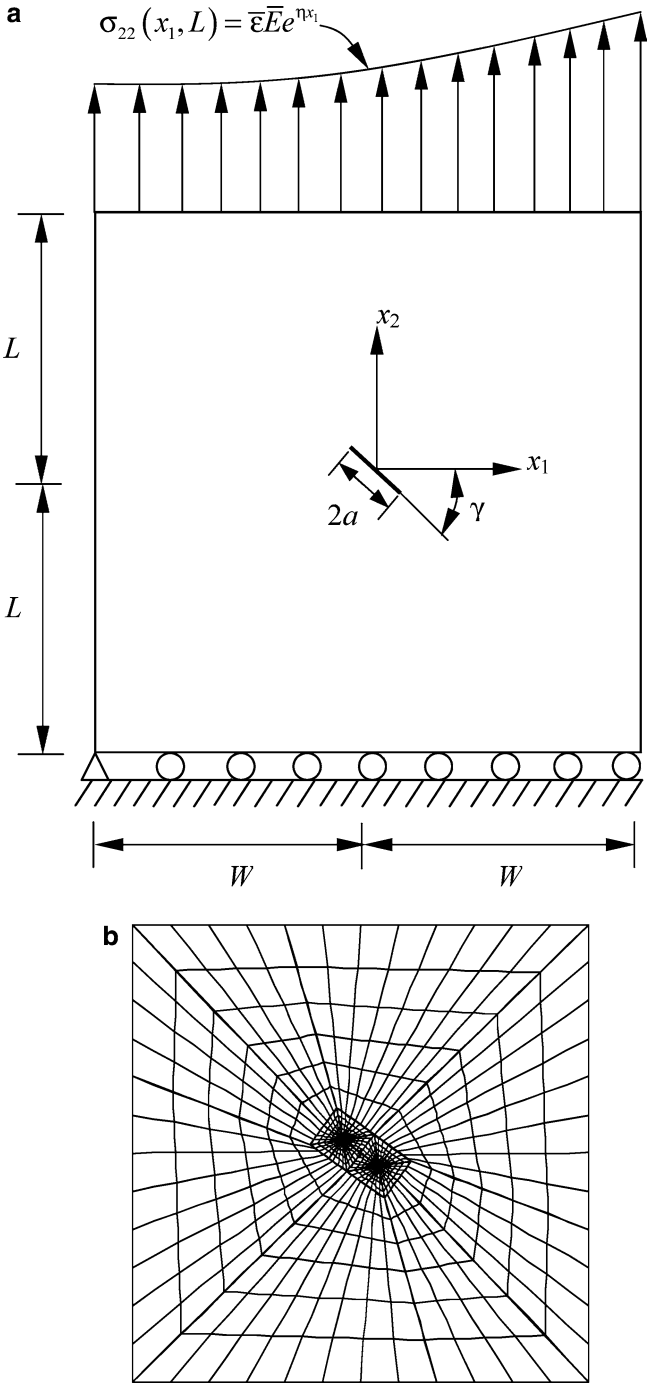

Fig. 10 Plate with an interior inclined crack under mixed mode loading; (a) Geometry and loads; and (b) FEM discretization for $\gamma/\pi = 0.2$

7 Summary and conclusions

A new continuum shape sensitivity method was developed for calculating mixed-mode stress-intensity factors for a stationary crack in two-dimensional, linear-elastic, isotropic FGMs having an arbitrary geometry. The method involves the material derivative concept taken from continuum mechanics, the mutual potential energy release rate, and direct differentiation. Since the governing variational equation is differentiated prior to discretization, the resulting sensitivity equations are independent of approximate numerical techniques, such as the finite element method, boundary element method, mesh-free method, or others. The discrete form of the mutual potential energy release rate is simple and easy to calculate, as it only requires multiplication of displacement vectors and stiffness sensitivity matrices. By judiciously selecting the velocity field, the method only requires displacement response in a subdomain close to the crack tip, thus rendering it computationally efficient. Seven finite-element based numerical examples, which comprise mode-I and mixed-

Table 8 Normalized stress intensity factors for a plate with an interior inclined crack ($\eta = 0.25$)

Method	γ/π	$\frac{K_I(+a)}{\bar{E}\bar{\varepsilon}\sqrt{\pi a}}$	$\frac{K_I(-a)}{\bar{E}\bar{\varepsilon}\sqrt{\pi a}}$	$\frac{K_{II}(+a)}{\bar{E}\bar{\varepsilon}\sqrt{\pi a}}$	$\frac{K_{II}(-a)}{\bar{E}\bar{\varepsilon}\sqrt{\pi a}}$
Present method	0	1.216	0.845	0	0
	0.1	1.097	0.767	−0.330	−0.254
	0.2	0.788	0.561	−0.524	−0.424
	0.3	0.415	0.298	−0.512	−0.438
	0.4	0.119	0.078	−0.307	−0.281
	0.5	0	0	0	0
Konda and Erdogan [26]	0	1.196	0.825	0	0
	0.1	1.081	0.750	−0.321	−0.254
	0.2	0.781	0.548	−0.514	−0.422
	0.3	0.414	0.290	−0.504	−0.437
	0.4	0.121	0.075	−0.304	−0.282
	0.5	0	0	0	0

Table 9 Normalized stress intensity factors for a plate with an interior inclined crack ($\eta = 0.5$)

Method	γ/π	$\frac{K_I(+a)}{\bar{E}\bar{\varepsilon}\sqrt{\pi a}}$	$\frac{K_I(-a)}{\bar{E}\bar{\varepsilon}\sqrt{\pi a}}$	$\frac{K_{II}(+a)}{\bar{E}\bar{\varepsilon}\sqrt{\pi a}}$	$\frac{K_{II}(-a)}{\bar{E}\bar{\varepsilon}\sqrt{\pi a}}$
Present method	0	1.433	0.689	0	0
	0.1	1.289	0.632	−0.358	−0.206
	0.2	0.921	0.472	−0.559	−0.361
	0.3	0.483	0.255	−0.539	−0.394
	0.4	0.142	0.064	−0.316	−0.266
	0.5	0	0	0	0
Konda and Erdogan [26]	0	1.424	0.674	0	0
	0.1	1.285	0.617	−0.344	−0.213
	0.2	0.925	0.460	−0.548	−0.365
	0.3	0.490	0.247	−0.532	−0.397
	0.4	0.146	0.059	−0.314	−0.269
	0.5	0	0	0	0

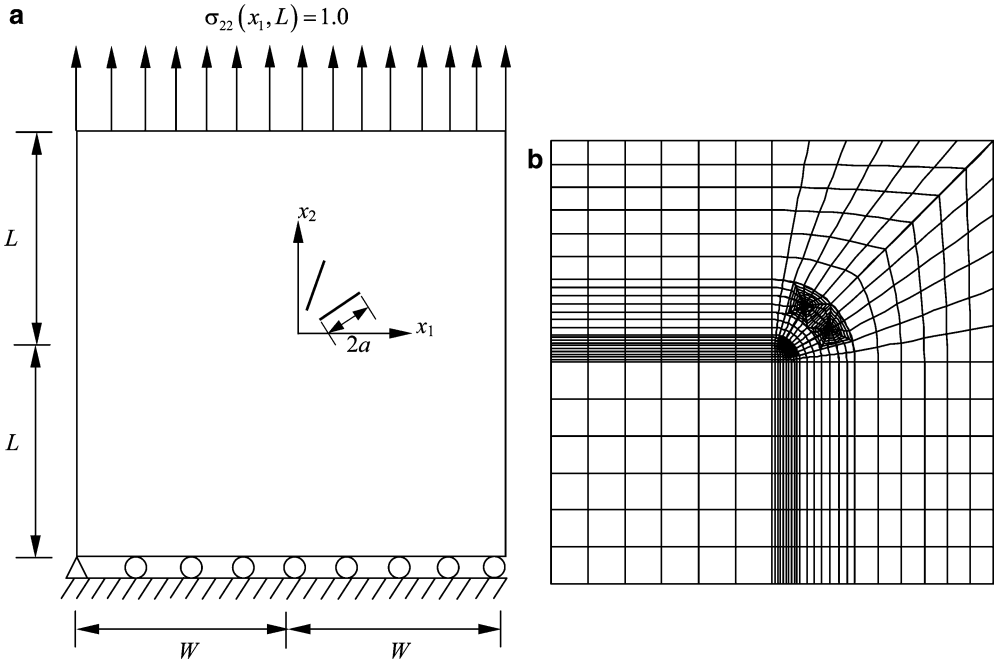

Fig. 11 Plate with two interacting cracks under mixed mode loading; (a) Geometry and loads; and (b) FEM discretization

mode deformations and/or single or multiple interacting cracks, are presented to evaluate the accuracy of fracture parameters calculated by the proposed method. Comparisons have been made between the stress-intensity factors predicted by the proposed method and available reference solutions in the literature, generated either analytically or numerically using various other fracture integrals or analyses. An excellent agreement is obtained between the results of the proposed method and previously obtained solutions. Therefore, shape sensitivity analysis provides an attractive alternative for fracture analysis of cracks in homogeneous and non-homogeneous materials.

Acknowledgements The authors would like to acknowledge the financial support of the U.S. National Science Foundation (NSF) under Award No. CMS 0409463.

References

1. Suresh S, Mortensen A (1998) Fundamentals of Functionally Graded Materials. IOM Communications Ltd., London
2. Erdogan F (1995) Fracture Mechanics of Functionally Graded Materials. Compos Eng 5(7):753–770
3. Paulino GH (2002) Fracture of Functionally Graded Materials. Eng Fract Mech 69(14–16):1519–1520
4. Rao BN, Rahman S (2003) Meshfree Analysis of Cracks in Isotropic Functionally Graded Materials. Eng Fract Mech 70:1–27
5. Rao BN, Rahman S (2003) An Interaction Integral Method for Analysis of Cracks in Orthotropic Functionally Graded Materials. Comput Mech 32(1–2):40–51
6. Gurtin ME (1981) An Introduction to Continuum Mechanics. Academic Press, New York, NY
7. Céa J (1981) Problems of Shape Optimal Design. In: EJ, Céa J, Sijthoff and Noordhoff, Alphen a/d Rijn (eds) Optimization of Distributed Parameters Structures
8. Haug EJ, Choi KK, Komkov V (1986) Design Sensitivity Analysis of Structural Systems. Academic Press, New York, NY
9. Fuenmayor J, Dominguez J, Giner E, Oliver JL (1997) Calculation of the Stress Intensity Factor and Estimation of Its Error by a Shape Sensitivity Analysis. Fatigue Fract Eng M 20(5):813–828
10. Hwang CG, Wawrzynek PA, Tayebi AK, Ingraffea AR (1998) On the virtual crack extension method for calculation of the rates of energy release rate. Eng Fract Mech 59(4):521–542
11. Giner E, Fuenmayor FJ, Besa AJ, Tur M (2002) An implementation of the stiffness derivative method as a discrete analytical sensitivity analysis and its application to mixed mode in LEFM. Eng Fract Mech 69(18):2051–2071
12. Feijóo RA, Padra C, Saliba R, Taroco E, Vénere MJ (2000) Shape Sensitivity Analysis for Energy Release Rate Evaluation and Its Application to the Study of Three-Dimensional Cracked Bodies. Comput Methpd Appl M 188:649–664
13. Taroco E (2000) Shape Sensitivity Analysis in Linear Elastic Fracture Mechanics. Comput Method Appl M 188:697–712
14. Lee TW, Grosse IR (1993) Energy Release Rate by a Shape Design Sensitivity Approach. Eng Fract Mech 44(5):807–819
15. Bonnet M (2001) Boundary Element based Formulations for Crack Shape Sensitivity Analysis. Eng Anal Bound Elem 25:347–362
16. Chen G, Rahman S, Park YH (2002) Shape Sensitivity Analysis of Linear-Elastic Cracked Structures. ASME J Press Vess T 124(4):476–482
17. Chen G, Rahman S, Park YH (2001) Shape Sensitivity and Reliability Analyses of Linear-Elastic Cracked Structures. Int J Fracture 112(3):223–246
18. Chen G, Rahman S, Park YH (2001) Shape Sensitivity Analysis in Mixed-Mode Fracture Mechanics. Comput Mech 27(4):282–291
19. Eischen JW (1987) Fracture of Nonhomogeneous Materials. Int J Fracture 34:3–22
20. Anderson TL (1995) Fracture Mechanics - Fundamentals and Applications. Second Edition, CRC Press, Boca Raton, Florida
21. Choi KK, Chang KH (1994) A Study of Design Velocity Field Computation for Shape Optimal Design. Finite Elem Anal Desi 15:317–341
22. Erdogan F, Wu BH (1997) The Surface Crack Problem for a Plate with Functionally Graded Properties. J Appl Mech. 64:449–456
23. Kim JH, Paulino GH (2002) Finite Element Evaluation of Mixed Mode Stress Intensity Factors in Functionally Graded Materials. Int J Numer Meth Eng 53(8):1903–1935
24. Chen J, Wu L, Du S (2000) Element Free Galerkin Methods for Fracture of Functionally Graded Materials. Key Eng Mat 183–187:487-492
25. Gu P, Dao M, Asaro RJ (1999) A Simplified Method for Calculating the Crack Tip Field of functionally Graded Materials Using the Domain Integral. J Appl Mech 66:101–108
26. Konda N, Erdogan F (1994) The Mixed Mode Crack Problem in a Nonhomogeneous Elastic Medium. Eng Fract Mech 47(4):533–545
27. Shbeeb NI, Binienda WK, Kreider KL (1999) Analysis of the driving forces for multiple cracks in an infinite nonhomogeneous plate, Part I: theoretical analysis. ASME J Appl Mech 66:492–500
28. Shbeeb NI, Binienda WK, Kreider KL (1999) Analysis of the driving forces for multiple cracks in an infinite nonhomogeneous plate, Part II: numerical solutions. ASME J Appl Mech 66:501–506